Projector Compensation for Unconventional Projection Surface

by

Vignesh Sankar

A thesis
presented to the University of Waterloo
in fulfillment of the
thesis requirement for the degree of
Master of Applied Science
in
Systems Design Engineering

Waterloo, Ontario, Canada, 2018

This thesis consists of material all of which I authored or co-authored: see Statement of Contributions included in the thesis. This is a true copy of the thesis, including any required final revisions, as accepted by my examiners.

I understand that my thesis may be made electronically available to the public.

Statement of Contribution

The thesis is based on the following papers. I am the first author and have contributed to the implementation, experimentation, and writing of all the papers. The content of Chapter 4 has been taken from paper (1) and majority of the content presented in Chapter 5 has been documented in paper (2) & (3).

1. V. Sankar, A. Gawish, and P. Fieguth. "Impact of Training Images on Radiometric Compensation." *Journal of Computational Vision and Imaging Systems*. 3.1 (2017).

2. V. Sankar, A. Gawish, P. Fieguth, and M. Lamm. "Understanding Blur and Model Learning in Projector Compensation." *Journal of Computational Vision and Imaging Systems*. (2018).

3. V. Sankar, A. Gawish, P. Fieguth, and M. Lamm. "ILRC: Inversely Learned Radiometric Compensation." *IEEE Transactions on Visualization and Computer Graphics*. submitted in August, 2018.

Abstract

Projecting onto irregular textured surfaces found on buildings, automobiles and theatre stages calls for the development of radiometric and geometric compensation algorithms that require no user intervention and compensate for the patterning and colourization of the background surface. This process needs a projector–camera setup where the feedback from the camera is used to learn the background's geometric and radiometric properties. In this thesis, radiometric compensation, which is used to correct for the background texture distortion, is discussed in detail. Existing compensation frameworks assume no inter–pixel coupling and develop an independent compensation model for each projector pixel. This assumption is valid on background with uniform texture variation but fails at sharp contrast differences leading to visible edge artifacts in the compensated image.

To overcome the edge artifacts, a novel radiometric compensation approach is presented that directly learns the compensation model, rather than inverting a learned forward model. That is, the proposed method uses spatially uniform camera images to learn the projector images that successfully hide the background. The proposed approach can be used with any existing radiometric compensation algorithm to improve its performance. Comparisons with classical and state-of-the-art methods show the superiority of the proposed method in terms of the perceived image quality and computational complexity.

The modified target image from the radiometric compensation algorithm can exceed the limited dynamic range of the projector resulting in saturation artifacts in the compensated image. Since the achievable range of luminance on the background surface with the given projector is limited, the projector compensation should also consider the contents of the target image along with the background properties while calculating the projector image. A novel spatially optimized luminance modification approach is proposed using human visual system properties to reduce the saturation artifacts. Here, the tolerance of the human visual system is exploited to make perceptually less sensitive modifications to the target image that in turn reduces the luminance demands from the projector. The proposed spatial modification approach can be combined with any radiometric compensation models to improve its performance. The simulated results of the proposed luminance modification are evaluated to show the improvement in perceptual performance. The inverse approach combined with the spatial luminance modification concludes the proposed projector compensation, which enables the optimum compensated projection on an arbitrary background surface.

Acknowledgements

First and foremost, I would like to thank my supervisors, Prof. Paul Fieguth and Prof. David Clausi for their constant support, guidance, and motivation throughout my degree. In addition, I wish to thank my co-author Dr. Ahmed Gawish for his inputs and suggestions in writing papers and conducting research.

I want to thank Christie Digital Systems for providing equipment, workspace, and support for my research. I would also like to acknowledge the assistance of Mark Lamm from Christie Digital Systems for his insights and suggestions.

I would like to convey my gratitude to the Vision and Image Processing lab for creating a healthy environment to conduct research. I am also grateful to the Ontario Centres of Excellence — Voucher for Innovation and Productivity II (OCE-VIPII), the Natural Sciences and Engineering Research Council of Canada — Collaborative Research and Development (NSERC-CRD) for sponsoring this research.

My special thanks to Prof. Jeff Orchard and Prof. Bryan Tripp for taking their time to review my thesis and provide valuable feedback.

Finally, I would like to thank my parents, N. Sankar and S. Bhanumathi, and my sister, S. Mohana Priya, for their continuous support and encouragement.

Dedication

This is dedicated to my parents.

Table of Contents

List of Tables

List of Figures

Chapter 1

Introduction

1.1 Motivation

Projector technology [37, 58, 30, 28] has been revolutionized in the last decade and it continues to increase the achievable resolution and contrast ratio of modern projectors. The power consumption and size of the projectors is also reducing dramatically [17] to make the projectors more portable. The rapidly increasing availability of high-end portable projectors has led to the increased use of three-dimensional objects, such as buildings, automobiles, and artistic structures, as projection surfaces for high-definition displays. Currently, projectors are used in every automobile show to highlight various features of a car. Projectors are also used during ceremonies and in theaters to dynamically change the perception of the scene on the stage. Niagara falls is regularly illuminated by the high–end laser projectors to attract more visitors during holidays. Disney theme parks are well known for using large scale projections as a part of their entertainment. On a smaller scale, projection technology can be used with 3D objects to create non-intrusive virtual reality experiences. Museums and art exhibitions have used this technology to restore the appearance of degraded artistic structures. Also, the emergence of the pocket sized pico projectors [17] has led to widespread use of projectors in households. Pico projectors are an affordable option to achieve High–Definition theatre experience on the go. More and more people are opting for the affordable high-end projectors, instead of a traditional LCD screen, for media consumption.

The ubiquitous use of projectors in households is only limited by the unavailability of projection screens. To obtain the stated resolution and contrast, a high quality projection screen is needed for the entire projection area. The currently available projection

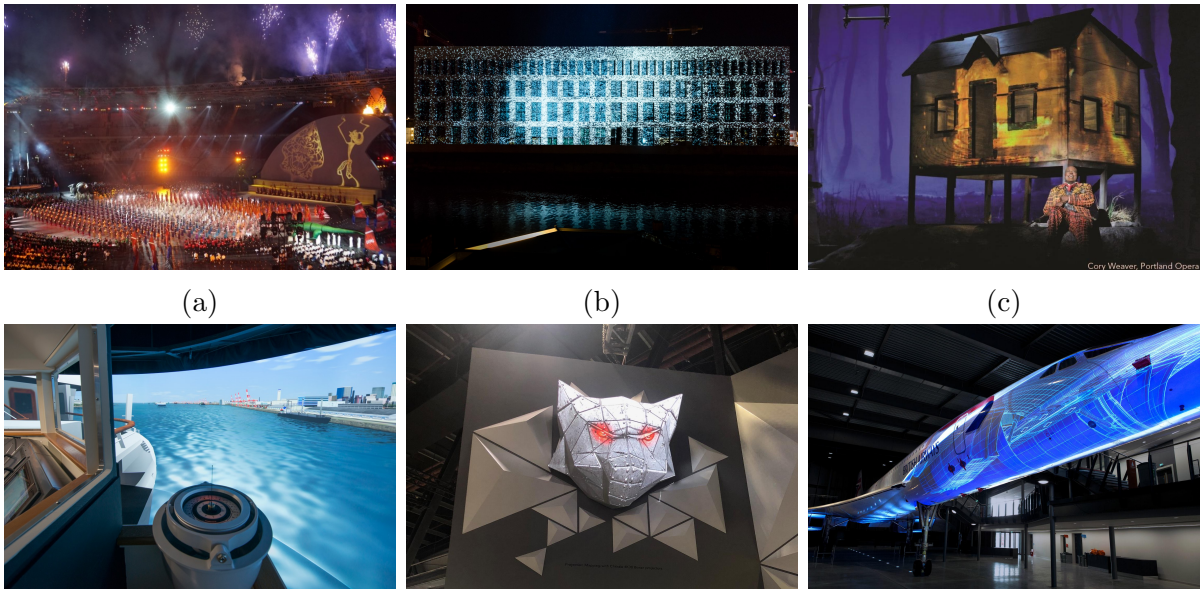

(a) (b) (c)

(d) (e) (f)

Figure 1.1: Application of the projection technology by Christie Digital Systems in (a) 2018 Asian paralympic games, (b) illumination of Berlin palace, (c) theatre illumination, (d) 360-degree ship bridge simulator, (e) 3D projections and (f) to restore a decommissioned plane[1]. The projector technology is successful in compensating for the 3D nature of the underlying object. However, the texture of the surface is still causing visible artifacts in the projection.

screens are substantial in size and are commonly expensive for household usage. Hence there is a need for modern projectors to shift from using a traditional projection screen to a nearby surface for projection. Using an arbitrary surface requires manual calibration to correct for image distortions. For projection on non-planar and 3D objects, projectors use geometric calibration to model the shape of the object and correct for structural distortions. However, modern projectors fail to compensate for the background texture. Existing approaches use high luminance projectors to mask the background texture, which is expensive. Otherwise, manual calibration is needed to neutralize the distortions, which consumes an enormous amount of time. Image processing techniques[47, 27] can be used to automatically understand the surface characteristics and use it to modify the target image such that un-distorted projections can be obtained on the surface. In this thesis, we explore different image processing techniques which can be used to develop automatic real–time projector compensation without human interference.

1.2 Problem Statement

Projector compensation is the process of achieving un–distorted image or video on a non-planar and textured background. It involves correcting for the geometric and radiometric distortions of the background. A projector–camera setup is used to understand the required surface properties [47]. A geometric model is developed from the learned properties that define the structure of the surface from the view point of the camera [53, 6, 31]. Geometric calibration results in an un–distorted image on the background surface which is degraded by the underlying texture of the surface. Radiometric compensation, which can correct for the texture degradation, is developed by projecting and capturing a series of colored images and using them to understand the surface's texture properties [47, 27, 64]. The compensation model, developed from the learned properties, modifies the intensities of the image with respect to the background such that the modified image combines with the background surface to present the desired image without any degradation. In case of a radiometrically extreme background surface or a limited dynamic range projector, image enhancement techniques [60, 26, 30] can be used as a part of projector compensation to reduce the brightness demands on the projector and obtain an optimum projector performance.

Geometric calibration is a well studied problem and current state of the art models can achieve sub-pixel accuracy from the camera viewpoint [63, 39]. Radiometric compensation is developed on top of the given geometric calibration model. The current radiometric framework uses a pixel–based approach, where a compensation function is developed for each projector pixel. Each compensation model is developed independently and the framework assumes no inference between adjacent pixels [47, 25]. This assumption works for background surface with smooth texture variations but fails at the background edges with sharp contrast difference [47].

The main aim of projector compensation is to reduce the perceptual difference between the desired target image and the compensated image on the background surface. Since the corrections are made with respect to the camera, the objective is to reduce the error between the target image and the compensated camera image. Two types of errors are encountered during compensation: the radiometric error, due to the incorrect learning/modelling of the background properties, and the saturation error, because of the physical limitations of the projector [28]. The projector compensation framework should be designed to minimize both radiometric and saturation error. The objective of this thesis is to provide a robust projector compensation framework, which can be used with any projector and camera

[1]Images are taken from Christie Digital Systems linkedin page:
https://www.linkedin.com/company/christie-digital-systems/

to provide the perceptually optimum projection of the desired image on any background surface.

1.3 Thesis Contribution and Organization

The next chapter reviews the current literature on different components of the projector compensation framework. State of the art models for the camera, projector and geometric calibration are provided. Different radiometric compensation models are discussed by categorizing them into the linear and non-linear model. Various image enhancement techniques which are proposed for improving the perceptual performance of the projector compensation are also discussed.

The projector–camera setup required for the compensation framework is discussed in Chapter 3. The necessary camera and projector calibration to be performed as a part of the experimental setup is elaborated. Since the camera forms the eye of the setup, the influence of camera parameters on the performance of the compensation model is examined in detail.

Chapter 4 discusses the assumptions of the existing radiometric compensation algorithms. Notably, the assumption of no interference between pixels is examined in detail. Experimental verification was provided by developing the same radiometric compensation model with different calibration sets to prove that the assumption will lead to artifacts at the background texture's edge.

Inspired from the results of Chapter 4, a novel inverse framework is proposed in Chapter 5, which can be used with any radiometric compensation algorithm to improve its performance. The proposed framework inherently learns the inter–pixel dependencies without an increase in computational complexity. The results of the inverse model are compared with the linear and state of the art non-linear models to justify the improvement in performance.

To reduce the brightness demands of the projector, a novel luminance modification approach is proposed in Chapter 6. Here, the modification is localized and spatially optimized for the human visual system. This approach can be used with the proposed or existing radiometric models to reduce artifacts due to device limitations. The combination of the inverse model with the spatially optimized luminance modification concludes the proposed projector compensation framework.

Chapter 2

Literature Review

2.1 Introduction

Radiometric compensation is the process of manipulating the incoming image to a projector such that the projected image modulates with the background to provide the desired appearance for an observer. This process utilizes a projector–camera system such that the projector projects an image onto the background surface, and the camera provides feedback in order to learn the geometric and radiometric properties of the surface. For a given target image, the compensated projector image is obtained by modifying the target image with respect to the learned properties. Projecting the compensated image gives the appearance of a non-distorted target image on the surface.

Imaging systems, such as camera and projector, have an inherent non-linear response while converting the digital intensity values to/from the scene irradiance. These responses are modelled as the radiometric response function. This chapter starts by reviewing the literature on the camera response function required for radiometric compensation. The geometric calibration needed to map the camera and projector image pixels are discussed in Section 2.3. Existing radiometric compensation along with the state of the art algorithms are discussed in detail. In conjunction with radiometric compensation, image enhancement techniques are proposed in the literature to improve the perceptual quality of the compensated image. In general, the proposed techniques are used to reduce the saturation artifacts encountered due to the limited dynamic range of the projector.

2.2 Camera and Projector Response Function

In most imaging systems [22], there is a non-linear relationship between the scene irradiance reading and the digital intensity values. The non-linearity can be due to the inherent gamma mapping in the device, analog/digital conversion, or introduced intentionally by the manufacturer to enhance the visual quality. Computer vision applications model the non-linearity as the response function of the device and uses it to establish linear relationship between the intensity values and scene irradiance. Extensive research has been done in the field of camera response functions [22, 24, 21, 23, 38, 21, 4, 33]. The most common approach uses a set of images captured with varying exposure values to calculate the camera response function [13, 41, 44]. Lin and Matsushita *et al.* [42] proposed to use noise distribution in the image to find the required function. Lee *et al.* [35] proposed a rank minimization framework to solve for the response function. Modern projectors have the manual setting to change the inherent non-linearity. But for traditional projectors, Grossberg *et al.* [25] proposed a framework to calculate the projector response function along with the radiometric compensation model assuming camera response function is known.

2.3 Geometric Calibration

After camera calibration with the radiometric response function, the geometric calibration between the projector and camera should be obtained. The pixel correspondence from the mapping is necessary to correlate the camera pixels to its corresponding projector pixels. The geometric calibration is calculated for a fixed projector–camera setup. Structured light patterns [53, 6, 31] are used to obtain geometric calibration for planar or non-planar textured backgrounds. Salvi *et al.* [53] provides a comprehensive review of the existing geometric calibration algorithms. Gray code structured light projection proposed by Inokuchi *et al.* [31] uses a sequence of m binary coded image pattern as shown in Fig 2.1 with hamming distance of one between images to encode 2^m pixels. Each pixel in the projector image is marked by the unique binary code and the captured camera image's pixels are decoded to find its corresponding projector pixel. Sansoni *et al.* [55] and Wiora *et al.* [63] proposed to use a combination of gray code and phase shift coding to achieve sub-pixel accuracy. The acquired geometric calibration between projector and camera is also used to compensate for the geometric distortion caused by the background surface.

In order to support dynamic projector–camera setting, Park *et al.* [48] embedded the structured light pattern with incoming projector images and simultaneously detected and

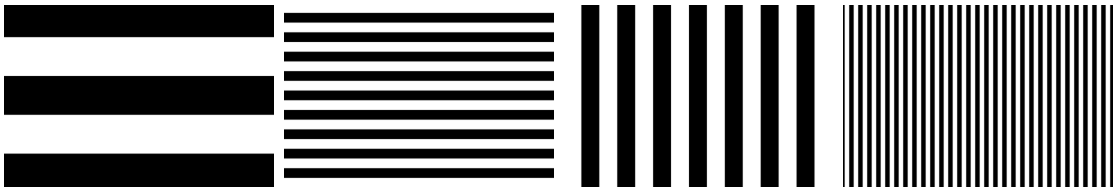

(a) Projector images

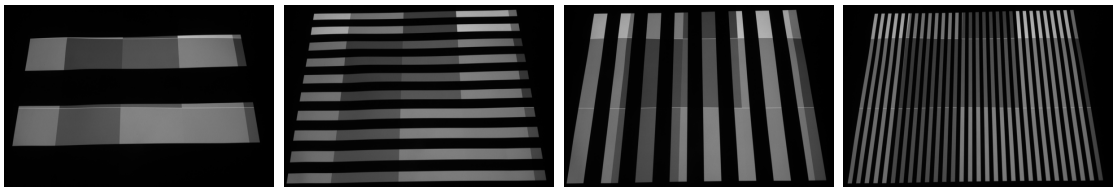

(b) Camera images

Figure 2.1: Examples of gray scale structured light pattern. Every pixel in the projector image is encoded using (a) the binary coded image sequence and (b) the camera image pixel values are decoded to find the corresponding projector pixel.

corrected for any change in projector–camera setup in real time. Recently, Bokaris *et al.* [8] proposed a robust calibration model by analyzing the characterization of DLP projectors, and proposed an algorithm which can achieve complete re-calibration with just one frame delay.

2.4 Radiometric Compensation

Radiometric compensation is required to correct for the projection image's texture distortion due to the background surface. To understand the surface's texture characteristics, a calibration set is formed by projecting a series of colored images and capturing their responses. The radiometric functions f_r developed from the calibration set, model the transformation of the projector image intensity $P(x_1, y_1)$ by the projection surface to produce the captured camera image intensity $C(x_2, y_2)$:

$$C(x_2, y_2) = f_r(P(x_1, y_1)) \tag{2.1}$$

Where projector image's pixel location at (x_1, y_1) corresponds to camera image's pixel location at (x_2, y_2). The function is developed for each projector–camera pixel pair, as

the background texture and colour can vary, essentially arbitrarily, from pixel to pixel. The radiometric function is inverted to form the compensation function f_r^{-1}, which can be applied to the target image intensity $T(x_1, y_1)$ to yield the compensated projector image intensity $P_c(x_1, y_1)$:

$$P_c(x_1, y_1) = f_r^{-1}(T(x_1, y_1)) \tag{2.2}$$

$$C_c = S(P_c) \tag{2.3}$$

where S represents the transformation by the background surface. C_c is the camera captured compensated image, ideally equivalent to the target image T. Since the radiometric function is developed for each projector pixel, it is necessary for the model to be simple and efficient. Different Models are used to define the different radiometric function depending on the scenario at hand. Broadly, radiometric functions can be categorized into either linear or non-linear models. The following subsection discuss each category in detail.

2.4.1 Linear Models

For a projector–camera system, Nayar *et al.* [47] proposed to model the input irradiance of the camera C_L for channel L in terms of the brightness output of the projector P_K for channel K as

$$C_L = \sum_K \int w_K(\lambda) S(\lambda) q_L(\lambda) P_K d\lambda \tag{2.4}$$

Here, w_K is the spectral response of the projector for channel K, S is the spectral reflectance of the surface in the viewing direction of the camera, and q_L is the quantum efficiency of the camera for channel L. The Projector I_P and Camera I_C pixel values are related to the irradiance values as follows,

$$P_K = r_P(I_P) \tag{2.5}$$

$$I_C = r_C(C_L) \tag{2.6}$$

where r_P and r_C represent the projector and camera response function. For a three color channel projector–camera system, (2.4) can be represented as

$$C = VP, \tag{2.7}$$

where

$$C = \begin{bmatrix} c_R \\ c_G \\ c_B \end{bmatrix}, \; V = \begin{bmatrix} v_{RR} & v_{RG} & v_{RB} \\ v_{GR} & v_{GG} & v_{GB} \\ v_{BR} & v_{BG} & v_{BB} \end{bmatrix}, \; P = \begin{bmatrix} p_R \\ p_G \\ p_B \end{bmatrix} \tag{2.8}$$

$$v_{KL} = \int w_K(\lambda) s(\lambda) q_L(\lambda) d\lambda \tag{2.9}$$

In principle the camera's and projector's spectral responses can overlap with each other in arbitrary ways [47], so it is necessary for the radiometric model to be able to capture all inter-channel dependencies. The model in (2.7) separates the non-linear projector/camera response function from the radiometric function and uses a linear system of equations to model the transformation of the projector brightness output. The color mixing matrix V captures the coupling of the camera and projector color channels and their interaction with the spectral reflectance of the background [47]. As with $f()$, the color mixing matrix V needs to be modelled separately for every projector pixel.

Yoshida *et al.* [64] improved Nayar's model in (2.7) by adding a constant term to consider the effects of environmental light and projector offset as

$$C = VP + K, \tag{2.10}$$

where

$$V = \begin{bmatrix} v_{RR} & v_{RG} & v_{RB} \\ v_{GR} & v_{GG} & v_{GB} \\ v_{BR} & v_{BG} & v_{BB} \end{bmatrix}, \; P = \begin{bmatrix} p_R \\ p_G \\ p_B \end{bmatrix}, \; K = \begin{bmatrix} k_R \\ k_G \\ k_B \end{bmatrix} \tag{2.11}$$

Bimber *et al.* [7] proposed a channel *in*dependent model, where the radiometric function is modeled as a diagonal matrix, thus the model does not consider the spectral response overlap between the projector and camera. Grossberg *et al.* [25] proposed to use a minimal set of six images to calculate the color mixing matrix V and projector response function.

Lee *et al.* [36] increased the speed of the radiometric compensation by eliminating the spectral overlap using color filters and modelling the color mixing matrix as a diagonal matrix. Chen *et al.* [10] studied the color mixing property of the projector–camera system and presented a method to separate the spectral overlap matrix from the color mixing matrix, where a single matrix was then calculated for the entire system to describe the spectral overlap between the projector and camera. Futji *et al.* [18] extended the linear model for dynamic environments by using a co-axial projector–camera system where the geometric correspondence between the projector and the camera is independent of environmental changes. Here, the color mixing matrix V was separated into a diagonal matrix A, which captures the spectral reflectance of the surface, and dense V_f, which represents the overlap between the projector and camera spectral responses:

$$C = AV_f P' \tag{2.12}$$

A is calculated for each projector pixel whereas, a single V_f matrix is used for all projector pixels. Mihara *et al.* [43] proposed a compensation model, which uses a high spatial

resolution camera to capture the background spectral reflectance variation inside a single projector pixel, such that Yoshida's linear model (2.10) is developed for each of the multiple camera pixels within a projector pixel.

The previously mentioned models assumes a Lambertian surface for the projection background. Park *et al.* [49] used multiple projectors and camera to use a non–Lambertian surfaces for projection. Here, the projectors are arranged such that at least one diffuse projector is available for each point at the projection surface which does not produce specular reflection for a given camera viewpoint.

2.4.2 Non-Linear Models

Chiu *et al.* [11] used the projector–camera system and a non-linear radiometric compensation model to remove the textured content on presenter's face during presentation. A non-linear radiometric model, based on (2.7), was presented along with an adaptation scheme for dynamic ambient light. The per-pixel linear model was extented to a cubic version as follows,

$$P' = \begin{bmatrix} p_{\text{cubic}} \\ p_{\text{quadratic}} \\ p_{\text{linear}} \end{bmatrix} \tag{2.13}$$

Grundhofer *et al.* [28, 27] proposed a non-linear compensation model, which does not require pre-calibration of the camera or projector response function. The algorithm uses a sparse sampling of the projector gamut and thin plate spline interpolation to generate the mapping from the projector's input image to output image of the camera in RGB space. The target image is automatically scaled to maximize the achievable luminance and contrast [28].

Both linear and non-linear models assume each camera pixel intensity depends on only one projector pixel intensity and environmental light. But in practical scenarios, there is inter–pixel coupling between projector pixels resulting in many-to-many relationships between the projector and camera. The limitations of the discussed radiometric compensation models are discussed in Chapter 4.

2.5 Image Enhancements

The compensated projector image P_c calculated from the linear or non-linear model does not consider the physical limitations of the projector or camera. In practical scenarios, P_c

intensity values can go beyond the dynamic range of the projector. The projector clips the image values at its limits and projects a saturated image. Since the required brightness is not projected on the given background, the compensated camera image C_c deviates from the target image leading to artifacts at the saturated regions. The saturation artifacts are not due to the incorrect learning of the background surface, and are caused by the limited dynamic range of the projector.

2.5.1 Multi–Projector Setup

Different approaches are proposed in the literature to solve for saturation artifacts. Multiple projectors can be used to solve for the limited dynamic range of a single projector, by using more then one projector to attain the required brightness level that hides the background texture. Bimber *et al.* [7] proposed to use multiple projectors, where the required brightness is distributed evenly among all the overlapping projectors for a given point on the projection surface. Miyagawa *et al.* [45] used state equations, which are controlled using camera feedback, to distribute brightness among multiple projectors. Tsukamoto *et al.* [59] came up with multiple projector brightness distribution framework using two Degree of Freedom (DOF) control structure. Here, the communication bandwidth is optimized by using a centralized feed–forward mechanism. Theoretical and experimental verification was provided to demonstrate the successful performance in still and moving images.

2.5.2 Gamut Mapping

Multiple projectors can effectively solve the limited brightness capability of a single projector, but it also increases the overall complexity and cost of the required setup. Saturation artifacts can be reduced with a single projector by modifying the contrast of the incoming images to fit inside the projector gamut. Ashdown *et al.* [5] presented a five stage framework where the target image is first converted to a perceptual uniform CIELUV color space. Chrominance and luminance fitting was carried out in the CIELUV color space, as linear change in this color space will lead to linear changes in perceptual sensitivity. The fitted target image is converted to RGB color space and combined with the radiometric compensation algorithms for projection. Park *et al.* [50] proposed to use a local adaptive mapping depending on the projection surface and target image intensity for each pixel. The adaptive mapping function is constrained to have smooth variation across pixels to avoid abrupt color changes. Huang *et al.* [29] decoupled the surface reflectance properties

from the color mixing matrix and then proposed luminance reallocation to solve for the clipping errors.

2.5.3 Anchoring Theory

Anchoring theory of lightness perception [19] is also used to solve for saturation artifacts. Luminance is a physical quantity which can be measured. Lightness, on the other hand, is a subjective brightness perceived by the human visual system. Lightness of a scene is determined by the brightest point of the scene or "anchoring point". The human visual system first spots the anchoring point and identifies it as white and then perceives the lightness of scene with respect to the anchoring point. Wang *et al.* [61] proposed to use the anchoring theory for brightness scaling and hue adjustments. The algorithm identifies and scales the value of the anchor point using the CIECAM02 [46] color appearance model. Huang *et al.* [30] extented the model and put forth a radiometric compensation framework using anchoring theory to reduce clipping errors and to improve the overall quality of the compensated image. Subjective tests were conducted to verify the superiority of the proposed framework.

2.5.4 Human Visual System

Ramasubramanian *et al.* [52] used human visual system properties derived from experimental data to calculate the threshold map of an image given its viewing conditions. The threshold map incorporates the luminance masking, contrast sensitivity and contrast masking properties to calculate the maximum possible luminance deviation for a particular pixel until the human visual system notices the difference. This threshold is calculated for each pixel separately and combines together to form the threshold map. The properties of the threshold map was used by Wang *et al.* [60] to calculate the global scaling factor which optimizes the trade off between overall brightness and saturation artifact error. Grundhofer *et al.* [26] used the threshold map to propose global and local changes to the target image to reduce the saturation artifact. The global changes depend on the saturation error and average luminance of the image. The local changes are calculated by the Gaussian smoothed saturation error and the changes are limited by the values from the threshold map. Temporal adaption for the global change is also provided as the part of the paper.

2.6 Summary

In this chapter, different components of the projector–camera system were discussed. Most commonly used camera response function and geometric calibration algorithms were presented along with recent advances. Linear and non-linear radiometric compensation algorithms were discussed in detail. Image enhancements methods used in combination with radiometric compensation models were categorized and state of the art solution in each category was explained. Next, Chapter 3 explains the projector–camera setup in detail. Chapter 4 discusses the common assumptions and limitations in the existing radiometric compensation models.

Chapter 3

Projector–Camera Setup

In the previous chapter, we discussed the state of the art radiometric compensation and image enhancement techniques. The compensation models require a projector–camera setup as shown in Fig 3.1. The camera provides continuous feedback of the projection, which can be used to learn the geometric and surface reflectance properties of the background. The learned properties are used to make corrections to the incoming image. Here, all the corrections are made with respect to the position and reading of the camera. For different position and viewing angles of the observer, the background reflectance properties of the projection surface changes. Hence, the developed geometric model is valid only near the camera viewpoint. As the observer moves away from the camera viewpoint, the compensated image starts to deviate from the desired image. Similarly, the radiometric corrections are made with respect to the intensity values captured by the camera. In this chapter, we discuss the parameters of the camera and their influence on the performance of the compensation. The details of the projector–camera setup used for the implementation of the geometric and radiometric models are also explained.

3.1 Camera Calibration

A 5M-pixel Gigabit Ethernet machine vision camera is used as a part of the projector–camera setup. The camera should be calibrated to have a monotonic response to the projector intensity values considering most of the existing radiometric models [47, 64, 25] assume a linear relationship between the projector and camera. Since cameras are developed to capture maximum details of the scene, different image processing techniques are embedded as part of the image capturing process [44]. One of the main purpose of

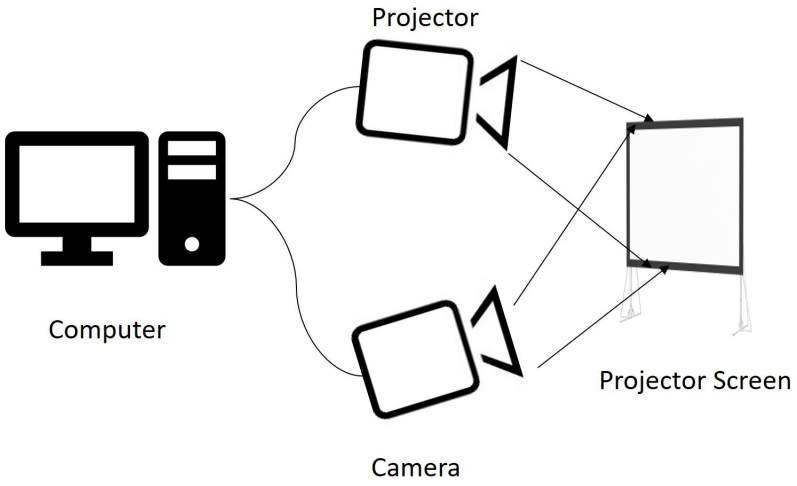

Figure 3.1: Projector–camera system for radiometric compensation. The camera provides a continuous feedback to understand the surface reflectance properties of the projector screen.

the embedded techniques is to automatically choose the white balance and exposure value of the camera. White balance defines the sensitivity of the RGB channels to different environmental conditions, which in turn affect the chrominance reading of the camera [3]. Different white balance settings lead to different chrominance readings of the static scene. Similarly, the exposure of the camera affects the luminance reading of the scene [34]. Automatic adjustment of white balance and exposure by the camera will lead to inconsistent readings. Most modern cameras come with "*automatic*" adjustment as the default setting for the white balance and exposure. In order to achieve monotonic response for projector values, we need to have constant white balance and exposure value. In Point Grey cameras, this was accomplished by manually changing the setting to have constant exposure and white balance value in the software provided.

Having constant white balance and exposure value ensures a monotonic response for the projector intensity values. In order to achieve a linear response, the camera's gain and gamma parameters values should be adjusted. Human perception of brightness approximately follows a power function, where the relative difference between the darker level of luminance is more sensitive than brighter levels [51]. The camera uses the following gamma correction to take advantage of the brightness perception property to optimize the bits usage while encoding an image:

$$V_{out} = V_{in}^{\gamma} \tag{3.1}$$

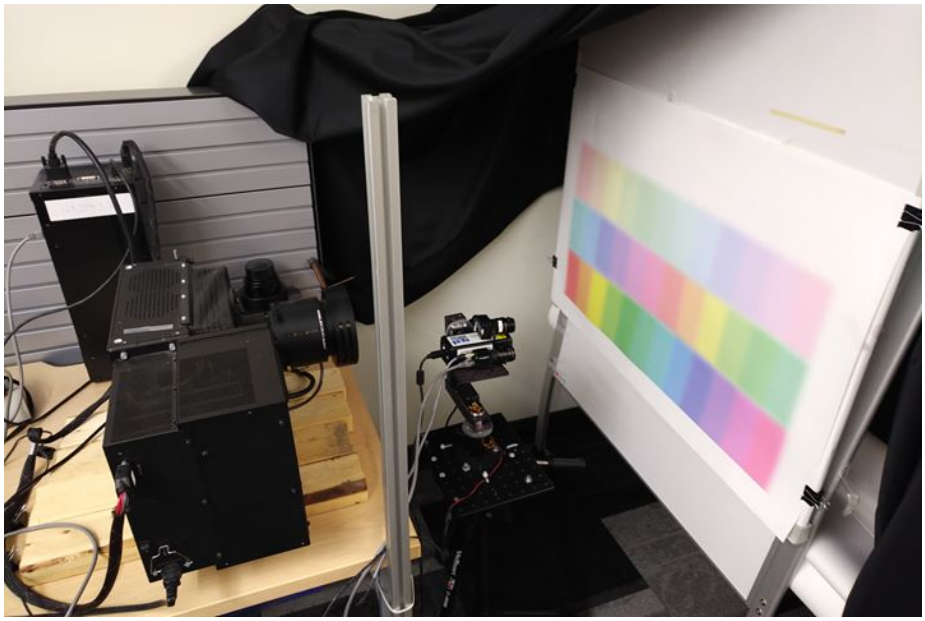

Figure 3.2: Projector–Camera system used for experiments

where V is the camera intensity value. The camera response functions [42, 35, 25] explored in Section 2.2 tries to model this gamma correction (3.1) of the camera. For the camera used in the experiments, we have manually set γ to 1 in order to avoid the non-linear transformation. Similarly, the gain of the camera [2] was set to 0 to avoid amplification. By manually adjusting the camera parameters, we avoided the need to calibrate the camera with the camera response function.

The linear response of the camera enables us to directly use the linear radiometric models discussed in Section 2.4.1. Since the compensation model uses the camera reading for correction, the exposure value of the camera plays a significant role in model performance. Different exposure values lead to different luminance readings of the same static scene [34]. Due to the limited dynamic range of the camera, an arbitrary exposure value can lead to saturation of camera reading and incorrect learning of the background properties resulting in artifacts in the compensated image. The aim of the camera is to capture the modulation of the projector intensity with the background surface. Hence, the camera's exposure value should be calibrated to capture the entire range of the achievable luminance on the background surface. In our experiments, the shutter speed was varied between 50ms - 100ms to control the exposure for different backgrounds.

The exposure values also act as the brightness parameter of the compensation image.

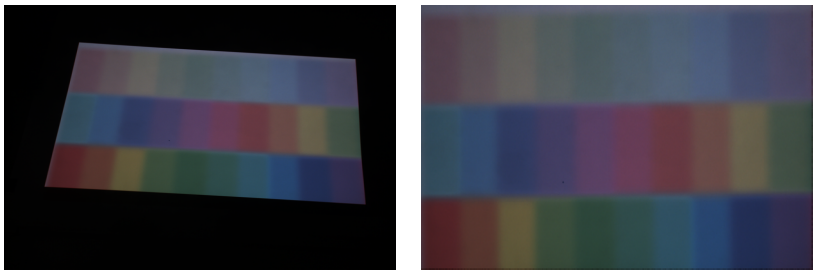

(a) Camera image (b) Transformed camera image

Figure 3.3: The transformation of the (a) camera image into (b) the projector coordinate system

The compensation model calculates the projector image value such that the modulation with the background results in the desired intensity value on the compensated camera image. A relatively higher exposure value will require low luminance demand from the projector to achieve the desired intensity in the camera image. As we reduce the exposure value of the camera and develop a new compensation model, the modified projector image brightness is increased to attain the same desired intensity in the camera image. Hence the brightness of the compensated image is inversely proportional to the exposure value of the camera. This property can also be used to avoid saturation of the projector image during radiometric compensation. The saturation of the projector is further discussed in Chapter 6.

3.2 Projector Calibration

The Christie Digital single chip 1920×1200 DLP projector was used in our projector–camera setup. The projector was connected to the computing device and used as a second monitor to project the image. The gamma modification by the operating system for display monitors was turned off to obtain a linear relationship between the projector and camera [1]. Similar to the camera, the non–linear transformation of the projector's gamma correction, was manually turned off to avoid the need for the projector response function.

3.3 Projector–Camera setup

The projector–camera setup of our experiment is shown in Fig 3.2. The camera is placed as close as possible to the projector to reduce the geometric distortions on the camera image. The entire setup was covered to ensure a minimum influence of ambient light. An example of a camera image is shown in Fig 3.3. To extract meaningful background property from the camera image, we require the camera–to–projector pixel location mapping. The pixel correspondence was acquired from the geometric calibration process. The gray scale structured light pattern [31] was used to obtain the geometric calibration as described in Section 2.3. The calibration will help in transforming the camera image to the projector coordinate system as shown in Fig 3.3. Having both the projector and camera image in the same coordinate system helped us to directly compare the images and extract background properties. This transformation was also used to calculate the error between the compensated camera image and the target image. The existing radiometric compensation frameworks [47, 27, 22] use pixel–level models developed for a static projector–camera setup. Any change in the projector–camera setup will lead to incorrect pixel correspondence and an ineffective compensation model. So the setup should remain static between model development and compensation. The same projector–camera setup is used for all of the experiments described in the following chapters.

Chapter 4

Limitations of Radiometric Compensation

We wish to examine the basic assumptions underlying the existing radiometric models and their implications on the performance of the associated radiometric compensation algorithms. The following assumptions are made in both the linear and non-linear radiometric models:

- The camera is capable of capturing the entire range of the projector gamut without saturation,
- Each camera pixel intensity is modelled as a function of only one projector pixel intensity,
- Environmental light is constant during model development and validation.

The camera plays a significant role in radiometric compensation as it forms the eye of the projector–camera system, and corrections to the projector image are made with respect to the values of the camera image. The visual quality of the radiometric compensation strongly depends on the ability of the camera to accurately capture the intensity and contrast of the background surface. Due to constraints on the portability and cost of the projector–camera system, off-the-shelf cameras with limited dynamic range are frequently used in practical scenarios, and as a result the camera could become saturated and might not be able to capture the entire range of the projector gamut. This saturation in the calibration images would lead to artifacts in the compensated image.

The radiometric function is developed for a static projector, camera, background and environment. Recent advances have led to use of dynamic projection using a coaxial projector and camera setup and real time geometric calibrations [18]. But existing algorithms still assume constant environmental light during radiometric function development and evaluation. Outdoor projection or indoor projection with changing environmental brightness can cause artifacts in the compensated camera image depending on the degree of brightness variation.

In the projector–camera system, the luminance of one projector pixel can influence the irradiance reading for multiple camera pixels, known as inter–pixel coupling [40], caused by one or more of

- Projector optics,
- Projection surface, or
- Camera optics.

That is, a single projector pixel may affect a neighbourhood of camera pixels, and similarly a camera pixel intensity may be a function of a neighbourhood of projector pixels. The inter–pixel coupling makes the projector–camera system a many-to-many relation, over some window size, where the extent of the window is determined by the nature or extent of the inter–pixel coupling. Under this scenario, the forward approach fails, as the inverse of the projector to camera transformation is not the same as the camera to projector transformation. Hence, there is a need to find a more suitable approach to successfully produce the target image on the background surface.

In this chapter, we look into the inter–pixel coupling in detail. The following section discusses the brightness leakage which can be observed in the projector–camera setup due to the inter–pixel coupling. The theoretical explanation is given for inter–pixel coupling by stating that the projector point spread/blur function can distort the projector images. Experimental verification is provided by developing the widely used Yoshida's [64] radiometric compensation model in Eqn. (2.10) using different sets of projector images and evaluating its performance under textured and plain background surface.

4.1 Brightness Leakage

For the background shown in Fig. 4.1a, let us consider the case in which only part of the background screen is illuminated, as shown in Fig. 4.1b, which gives rise to the camera

(a) Background (b) Projected image (c) Histogram equalized camera image

Figure 4.1: Brightness leakage of the projector–camera system can be seen by (b) illuminating a part of the projector screen and by (c) examining the histogram equalized camera image of the projector screen. The illuminated regions affect the intensity reading of the surrounding non-illuminated regions.

image of Fig. 4.1c, which has been histogram equalized [20] to bring out details. Although only a square region was formally illuminated, the luminance of the illuminated region is very obviously leaked to adjacent non-illuminated regions, including pixels quite some distance away. As a result, the captured values in the non-illuminated regions are not an appropriate function of the corresponding projector intensity since the radiometric model, which does not consider inter–pixel coupling, associates these values as a contribution from the background texture. The brightness leakage which is prominent at the projector image edges or the background's texture edges causes incorrect learning of the radiometric model and leads to visible edges in the compensated camera images.

The results of Yoshida's [64] linear model are shown in Fig. 4.2, from which it can be observed that the linear model is able to compensate satisfactorily in uniform regions, but the edges of the background remain visible in the compensated camera image. The pixel intensities in a horizontal cross-section of the compensated camera image are plotted in Fig. 4.3, showing that the compensated camera image intensity is deviating from the target intensity in the vicinity of edges in the projected background. Similar effects can be observed for all of the edges in the compensated camera image. The difference between the target image and compensated camera image is shown in Fig. 4.2d. Red indicates the positive values and green indicates negative values. We can observe significant deviation at all the background edges and the quantity of deviation is proportional to the contrast of the edge.

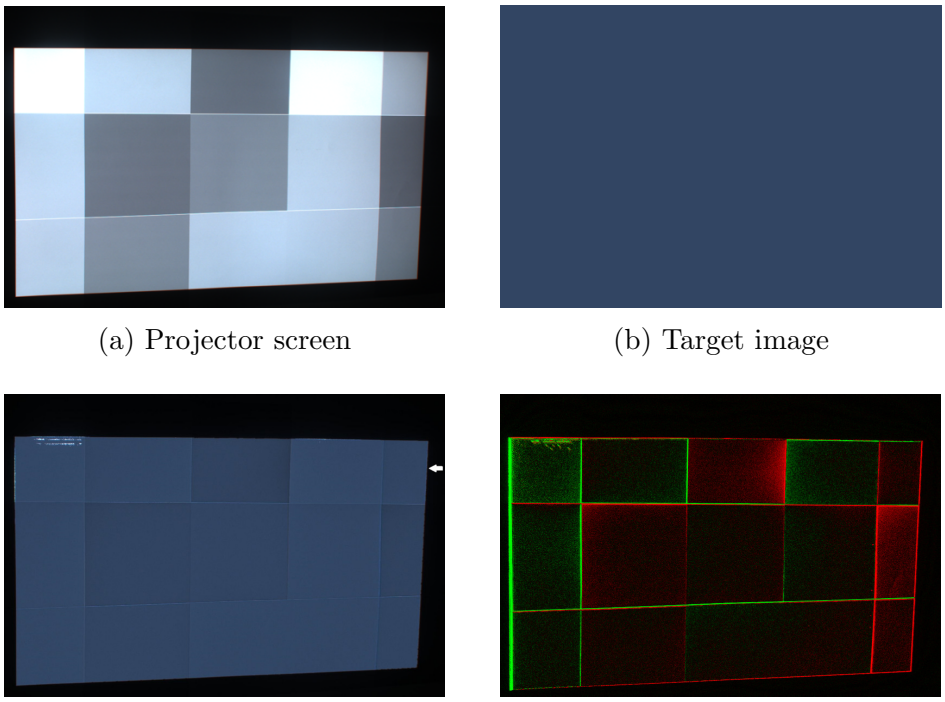

(a) Projector screen

(b) Target image

(c) Resulting compensated camera image

(d) Difference image (b) - (c)

Figure 4.2: Result of Yoshida's extended linear model. Edges of the background are clearly visible in the compensated result (c). The difference between the target and compensated image is plotted in (d), where red indicates positive values suggesting lower luminance in compensated image and green indicates negative values. The linear model works properly in the uniform region but fails near the regions of contrast difference. The arrow in the compensated camera image (upper right corner of (c)) identifies the row corresponding to the plot in Fig. 4.3.

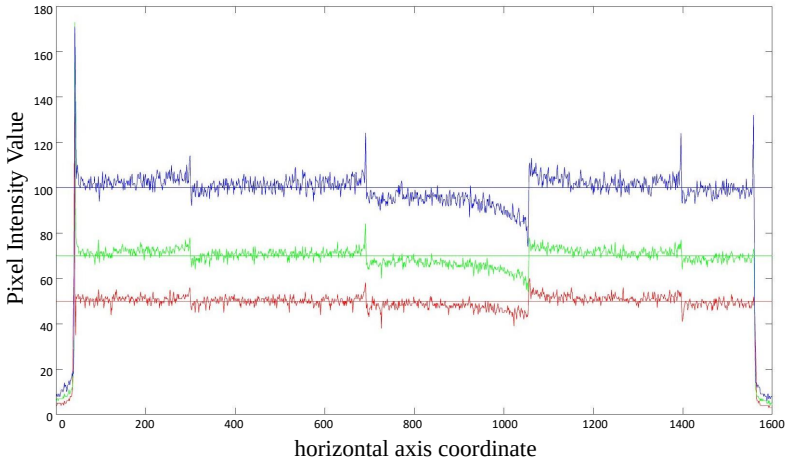

Figure 4.3: Distribution of camera image intensities along a horizontal row as indicated by the small arrow in Fig. 4.2c. The straight lines show the target values for each channel. Clearly visible are the sharp deviations from target near regions of contrast difference in the background.

4.2 Theoretical Analysis of Inter–Pixel Coupling

A major venue for inter–pixel coupling is at the projector. The point spread function of the projector can blur the input image creating spatial dependencies. Since the blur of the projector depends on the contents of the input image, different projector images in the calibration set can lead to different performance by the compensation model. For a spatially uniform projector image P_u, as shown in Fig. 4.4, the projector's blur function will not alter the intensities of the image:

$$B * P_u = P_u \tag{4.1}$$

As P_u does not contain any contrast, it will not be affected by the blur B. If the calibration set is developed with similar projector–camera images, the radiometric function $\hat{f}$ calculated from this set will not be aware of the blur function of the projector:

$$\begin{aligned} \hat{f} &= \arg\min_f \|f(P_u) - S(B * P_u)\| \\ &= \arg\min_f \|f(P_u) - S(P_u)\| \end{aligned} \tag{4.2}$$

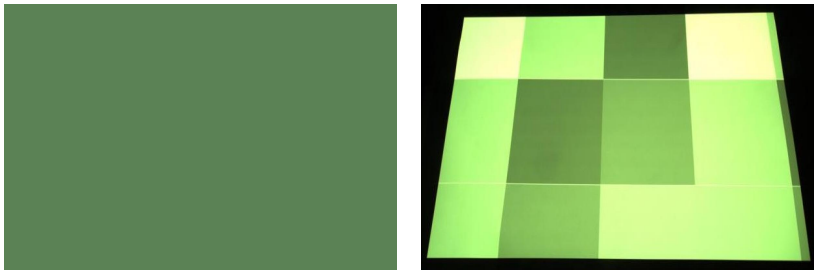

(a) Projector image (b) Camera image

Figure 4.4: Conventional calibration set with spatially uniform projector image and camera image of the projection.

where S represents the distortions by the background surface. The compensated projector image P_c for a given target image T is calculated as follows,

$$P_c = \hat{f}^{-1}(T) \tag{4.3}$$

The calculated P_c, unlike the uniform projector images in calibration set P_u, will not be spatially uniform in intensity. As the radiometric compensation model did not consider the effect of B, distortion of the non-uniform P_c by the blur function B will necessarily lead to artifacts in the compensated camera image:

$$B * P_c \neq P_c \tag{4.4}$$

$$S(B * P_c) \neq S(P_c) = T \tag{4.5}$$

Using spatially uniform projector images in the calibration set can cause artifacts in the compensated camera image. Similarly, different kinds of projector images can lead to various artifacts. So to understand the relationship between the projector image pattern and the artifacts in the compensated image, we analyzed the error maps of the radiometric compensation model developed with different sets of projector images.

4.3 Experimental Observation

Two calibration sets were constructed to examine the influence of inter–pixel coupling. The first set contains textured projector images using natural pictures, whereas the second set is formed using spatially uniform projector images as shown in Fig. 4.5. The calibration sets are combined with two different backgrounds. Due to the projector's point spread

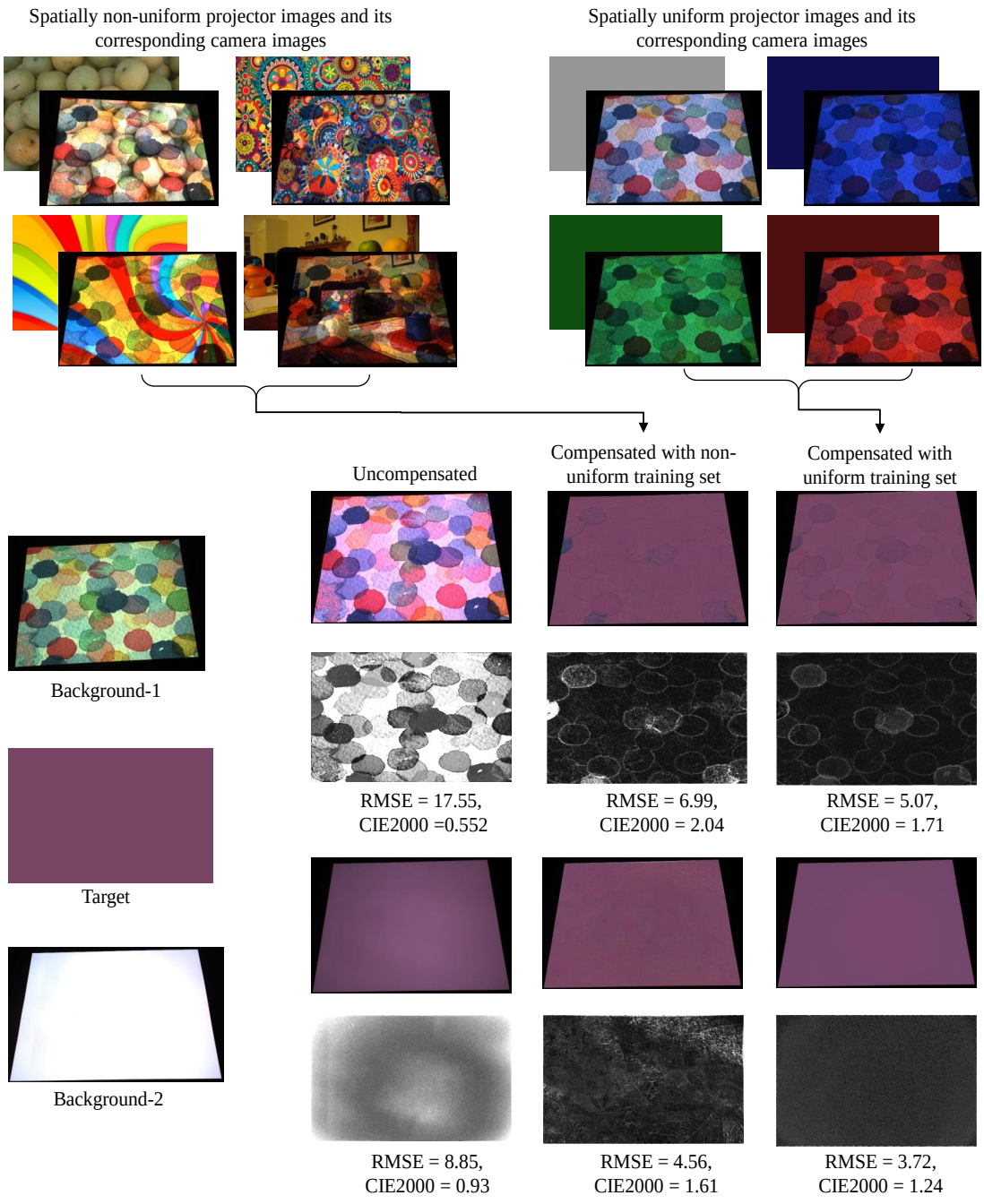

Figure 4.5: Comparison between direct projection and compensation by the linear model developed with spatially uniform and non–uniform calibration images. We can observe that the different types of calibration images lead to different patterns of artifacts on the compensated image.

function, each calibration sets should result in different radiometric compensation performance. By examining the pattern of artifacts in the compensated image with the pattern in the projector image and background, we can understand the influence of inter–pixel coupling. Here, four scenarios are explored:

- Plain calibration set with background-1
- Textured calibration set with background-1
- Textured calibration set with background-2
- Plain calibration set with background-2

Plain projector images without contrast are projected and captured by the camera to form the plain calibration set. Here, the projector images do not contain contrast difference, whereas the camera images contain the contrast difference of the corresponding background. The textured calibration set is composed of real world images as projector images and their corresponding camera images. Here, the camera images contain contrast difference from the projector images and the background texture.

The results of the experiments are illustrated in Fig 4.5. The RMSE error map between the target image and the compensated image displays the RMSE error for each projector pixel. The error map helps in identifying the pattern of artifacts in the compensated image. For background-2, which does not have any contrast difference, applying the linear radiometric compensation model gave different pattern of artifacts for plain and textured calibration sets. The plain calibration set's error map does not follow any pattern and contains random noise. The textured calibrations set's error map might seem arbitrary but careful observation shows that the pattern of the artifacts is an amalgamation of different contrast patterns present in the projector images. Fig. 4.6 highlights the similarity in detail: The pattern in different regions of the error map can be attributed to the pattern in projector images with the same spatial location.

From the results of background-1, we can observe that the plain training set is not able to hide the background texture. The linear model delivers satisfactory results in uniform regions, but deteriorates from the target in regions of contrast difference of the background. This phenomenon can be clearly observed in the RMSE error maps. In the absence of contrast in the projector images, the artifacts reflect the contrast pattern of the background. Using the textured calibration set with background-1 explains the performance of the radiometric compensation model in the presence of projector and background contrast. Here, the error map patterns are a combination of contrast from all the projector images and background texture.

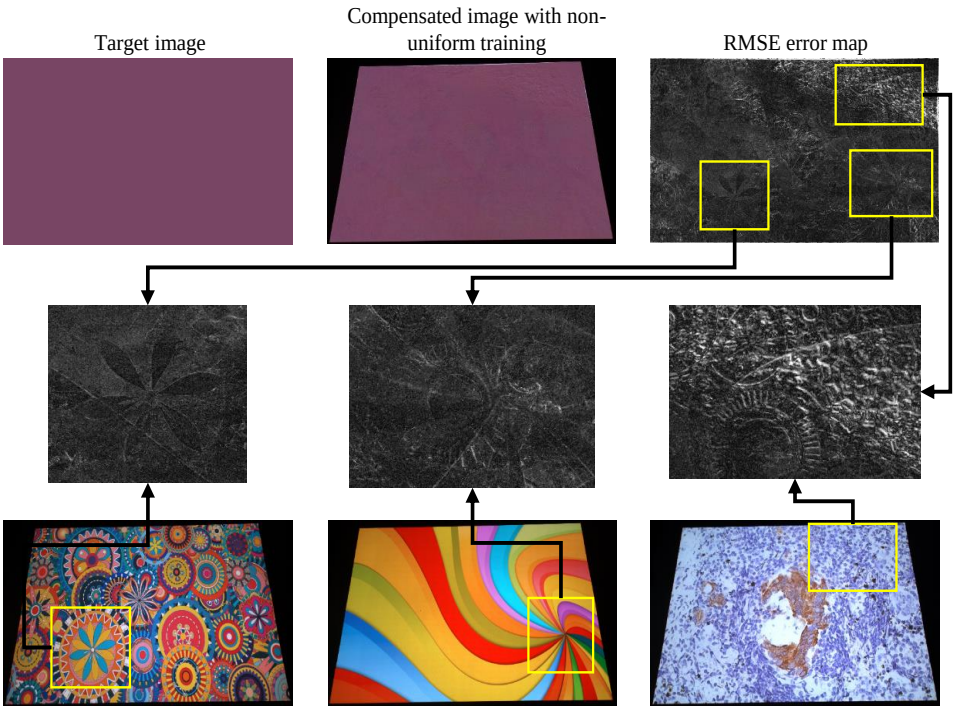

Figure 4.6: The contrast of the camera images in the calibration set (third row) is being reflected as artifacts in the compensated camera image. A closer look at the RMSE error map shows the artifact pattern is an amalgamation of the contrast present in the calibration set.

From the results, we can state that the artifacts due to inter–pixel coupling are a combination of contrast patterns from the projector images of the calibration set and background. Depending on the application scenario, the background pattern can vary arbitrarily, but we can control the pattern on the projector images. So we need a framework which can optimize the performance of the compensation model by using the most suitable calibration set.

Chapter 5

Radiometric Artifacts

The previous chapter discussed a key limitation of previously proposed radiometric models. In particular, that if smooth projector images are used in the calibration set, which give rise to spatially *non*-uniform camera images, then the contrast of these images will create artifacts at background edges. By somehow reducing the contrast of the camera images in the calibration set, the consequences of inter–pixel coupling can be reduced [54].

A novel inverse approach is proposed to overcome the limitations of inter–pixel coupling. A key strength is that the proposed approach can be applied to any existing radiometric compensation strategy to improve its performance. Since the radiometric model is developed for each pixel in the projector image, the changes are proposed in such a way that the model's complexity is not increased. In particular,

1. The compensation function is deduced directly, rather than inverting a learned radiometric function.
2. The calibration set is modified, consisting of spatially uniform *camera* images, allowing the compensation function to explicitly learn the projector pixel intensities needed to obtain spatially uniform camera images, maximally hiding the background.

The human visual system is sensitive to abrupt changes in intensity [26]. So the emphasis of the proposed model is to obtain smooth images on the projection surface which can completely hide the background texture. In the previous chapter, we studied the impact of calibration images on the performance of radiometric compensation. Due to the presence of inter–pixel coupling, existing radiometric compensation models produce artifacts with patterns similar to the pattern of camera images in the calibration set. So the proposed approach modified the calibration set to contain spatially uniform camera images.

The smooth camera images reduce the patterning of the artifacts leading to perceptually pleasing compensated images.

As in (2.1), now starting with a camera image C, the inverse model is given as

$$P = f_i(C) \tag{5.1}$$

C will be a spatially uniform fully compensated camera image, as shown in Fig. 5.2b, based on the corresponding projector image P. The existing radiometric function models the background's surface reflectance and inverts the model to find the compensation function. Due to the presence of inter–pixel coupling, the compensation function may not be equivalent to the inverse of the radiometric function. Hence, directly developing the compensation function from the calibration set gives the best estimate of the required function. By directly learning the inverse function f_i:

1. The need to model the brightness spread of the projector–camera system is avoided.
2. Any noise-amplification present in the model inversion stage of the forward approach is mitigated.

The proposed framework is developed with desired input–output pairs; by training with uniform camera images and their corresponding (non-uniform) projector images, the absence of texture in the uniform target images prevents artifacts distracting to the human visual system from appearing. Using uniform camera images C_u in the calibration set also lead to non-uniform projector images P_{nu}. So the compensation function calculated from the proposed calibration set includes the projector's blur effects, discussed in Section 4.1, during model learning as follows,

$$\hat{f}_i = \arg\min_{f_i} \|f_i(S(B * P_{nu})) - P_{nu}\| \tag{5.2}$$

The two proposed changes inherently learn the effect of inter–pixel coupling by making minimum changes to the existing radiometric compensation. The smooth camera images needed for the calibration set are acquired through an iterative approach. The iterative approach is only used in the offline process to form the calibration set. The next section discusses the iterative approach in detail.

5.1 Iterative Approach

One challenge, of course, is how to actually deduce the complex projector image, of Fig. 5.2, which actually corresponds to a smooth camera image.

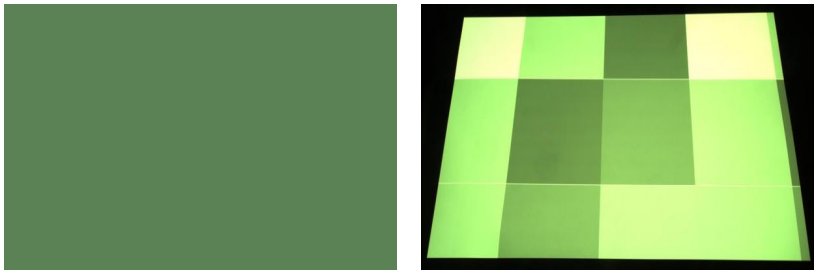

(a) Projector image (b) Camera image

Figure 5.1: Conventional calibration set with a spatially uniform projector image and its corresponding camera image.

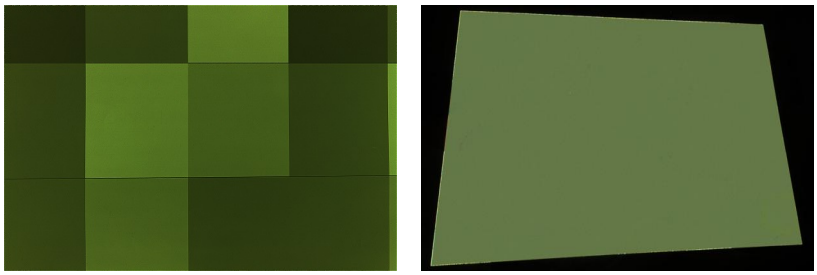

(a) Projector image (b) Camera image

Figure 5.2: In contrast to Figure 5.1, our proposed calibration set has spatially uniform camera images and a corresponding non-uniform projector image.

Since the goal of this research is to develop and explore the most effective strategies for radiometric compensation, rather than (for now) a fast and efficient algorithm, we have chosen a simple but highly robust and reliable iterative approach. The projector image at the first iteration is set to the target image,

$$P^0 = T \tag{5.3}$$

The resulting camera image C can measure the degree to which the target T is matched, but only after being converted to C_P in the coordinate system of the projector, based on the learned pixel correspondence. The resulting error or inconsistency between camera and target is easily calculated,

$$E^t = C_P^t - T \tag{5.4}$$

(a) Monochrome (b) Colored

Figure 5.3: Camera images of the two background projection screens used in the experiments.

on the basis of which each pixel in P can be updated to reduce the error, thus

$$P_{x,y}^{t+1} = \begin{cases} P_{x,y}^{t} + K, & \text{if } E_{x,y}^{t} < -\tau \\ P_{x,y}^{t} - K, & \text{if } E_{x,y}^{t} > \tau \end{cases} \tag{5.5}$$

for some minimum threshold τ. $K = 2$ and $\tau = 2$ were used during experiments.

The iteration is terminated when the average error across the image is below a preset threshold. In practice, the total number of iterations can be reduced by updating proportional to the error as

$$P_{x,y}^{t+1} = P_{x,y}^{t} - \gamma \cdot E_{x,y}^{t}, \tag{5.6}$$

for some rate of convergence γ. In practice, for $\gamma = 0.4$, It was found that 10 iterations are sufficient for convergence for the backgrounds shown in Fig 5.3.

By this means we can successfully create the calibration set with spatially uniform camera images. The iterative approach is only used in the calibration phase and will not affect the complexity during model evaluation.

Depending on the projector gamut, each background can be characterized with the achievable range of image intensities without projector saturation. The range of intensities in the camera images of the calibration set should be spread across this achievable dynamic range for a robust compensation model.

5.2 Experimental Setup & Results

In this section, the experimental setup required for the proposed framework is discussed in detail. The proposed framework is applied on the Yoshida's and Bimber's linear models to

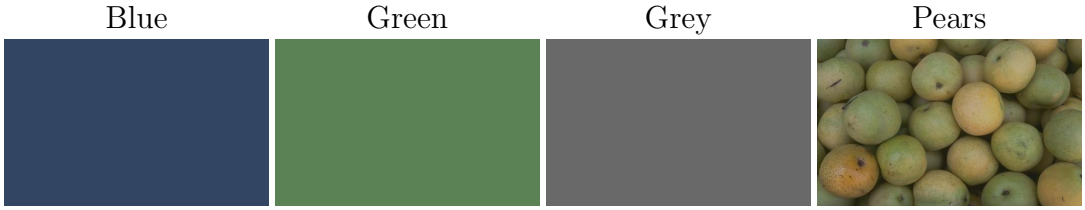

Figure 5.4: Target Images

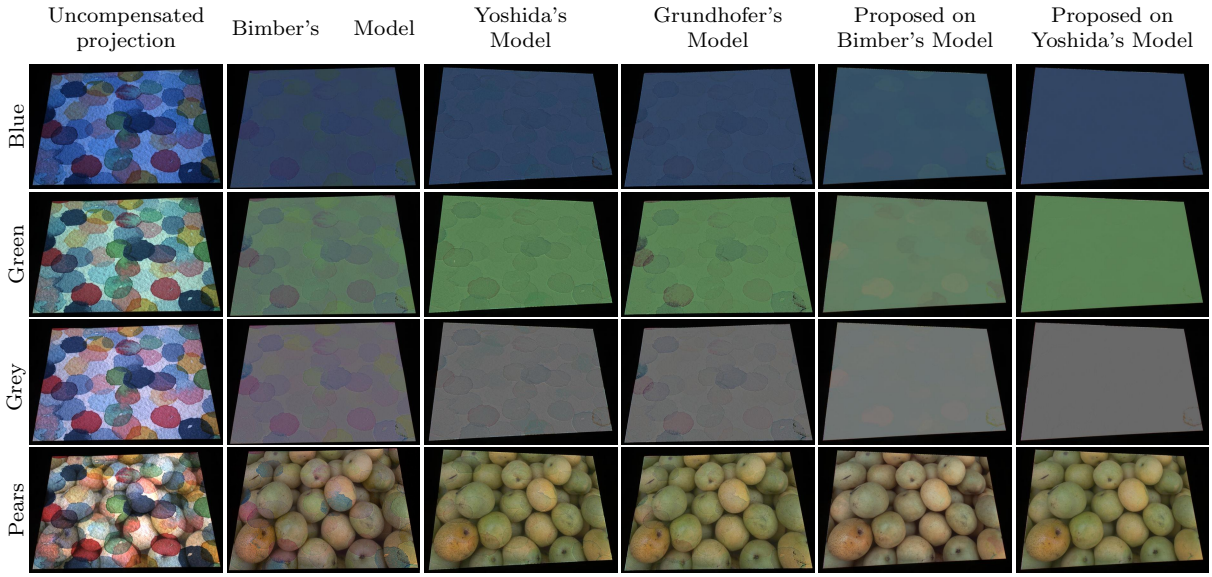

Figure 5.5: The results of the proposed changes applied to Bimber's and Yoshida's model are compared with existing models on the background shown in Fig. 5.3b. Note in particular the significant reduction in background contrast remaining in the compensated image in our proposed approach (last two columns) compared with established methods (middle three columns). The artifacts encountered at the bottom right of the proposed Yoshida's model is due to saturation which is discussed in Chapter 6

RMSE

Image	Uncompensated	Bimber	Yoshida	Grundhofer	Proposed Bimber	Proposed Yoshida
Blue	56.89	6.46	5.16	4.18	8.02	2.34
Green	71.24	12.96	7.14	5.22	10.63	3.42
Grey	76.85	7.92	7.01	5.37	10.46	3.06
Pears	70.46	8.11	7.49	4.39	9.20	4.08
15 Images (Avg.)	72.59	8.86	6.70	5.11	9.58	3.23

CIE2000

Image	Uncompensated	Bimber	Yoshida	Grundhofer	Proposed Bimber	Proposed Yoshida
Blue	17.78	3.60	1.63	1.51	6.99	0.98
Green	29.99	10.01	2.11	1.96	6.15	1.12
Grey	28.70	7.40	3.16	3.02	5.85	1.89
Pears	27.22	8.71	2.60	2.06	6.87	1.64
15 Images (Avg.)	20.54	5.75	2.07	1.96	6.78	1.24

SSIM

Image	Uncompensated	Bimber	Yoshida	Grundhofer	Proposed Bimber	Proposed Yoshida
Blue	0.715	0.966	0.987	0.989	0.973	0.995
Green	0.471	0.744	0.978	0.981	0.884	0.990
Grey	0.260	0.675	0.836	0.843	0.846	0.921
Pears	0.460	0.879	0.973	0.975	0.942	0.987
15 Images (Avg.)	0.455	0.802	0.914	0.921	0.879	0.974

Table 5.1: RMSE, CIE2000, and SSIM scores for the images in Fig. 5.5. In every single case, for every image and every metric, the proposed approach applied to Yoshida's method offers the best result.

improve its performance. The performance of the proposed model is then compared with the state of the art non-linear model to show its superiority.

5.2.1 Implementation

The projector–camera setup was installed as discussed in Chapter 3. After the linearization of the camera response with the projector intensity values, the gray scale coding algorithm [31] was used to find the pixel correspondence between the projector and camera. The nearest neighbour method was used to assert a location for projector pixels for which a corresponding camera pixel was not found. After geometric calibration, an iterative approach (5.5), (5.6) was used, typically requiring 8-12 iterations for each image, to form the calibration set. Intensity values for the calibration set were chosen from those intensity values which do not lead to any saturation in the projector, and a total of ten such projector–camera pairs were found. The proposed changes were applied to Bimber's [7] and Yoshida's [64] linear radiometric models to evaluate performance. The calibration image pairs were used to learn the inverse model, as proposed, and this model was calculated separately for each projector–camera pixel pair.

5.2.2 Comparison Methods

The proposed approach is compared with the un-modified Bimber's [7], Yoshida's [64] model, and Grundhofer's [28] non-linear model.

For Grundhofer's non-linear model, the calibration set is created by sampling each projector channel into N intervals. Combining the RGB channels of the projector, N^3 calibration images are obtained as described in [28]. In this paper, each channel was sampled into $N = 5$ intervals, resulting in 125 projector–camera images. Thin plate spline interpolation [15] with radial basis functions is used to model the transformation between the projector and the camera images, as given in [28]. A regularization term is added to the weights to reduce the measurement inaccuracies as proposed in [14]. The drift movement correction and global optimization for maximum luminance and contrast were not implemented as these were not a part of the radiometric compensation model [28].

For Yoshida's and Bimber's linear models, the calibration set of 20–30 pairs of projector–camera images was developed by choosing intensity values covering all three projector channels. Yoshida's and Bimber's radiometric models were developed as given in [64] and [7] respectively.

5.2.3 Evaluation Metrics

To compare the camera and target images, the camera images are converted to the projector's coordinate system using the acquired pixel correspondences. The CIE2000 ΔE^*_{00} [57], Root Mean Square Error (RMSE), and Structural Similarity (SSIM) [62] metrics were used in evaluating the compensation performance. The RMSE score

$$\|c, t\| = \sqrt{(c_r - t_r)^2 + (c_g - t_g)^2 + (c_b + t_b)^2} \tag{5.7}$$

between camera pixel c and target pixel t is calculated in the RGB color space, whereas CIE2000 is based on the device–independent CIEL*a*b* color space, intended to more accurately reflect human visual perceptual differences between colors.

Broadly speaking, there are two classes of artifacts which appear:

- Radiometric artifacts, due to some limitation in modeling or learning of the background, that results in the deviation of the camera image from the intended target.
- Saturation artifacts, which arise when the compensated projector intensity falls outside of the dynamic range of the projector.

Since our study is explicitly focused on radiometric compensation, only unsaturated pixel locations are considered for error calculation. The saturation artifacts are explored in detail in Chapter 6.

5.2.4 Results

The results of spatially uniform target images with two backgrounds are shown in Figs. 5.5 and 5.7. Here, the results of three different spatially uniform images are shown, since their uniformity represents the most challenging scenario when projecting onto an irregular background.

Even a casual glance at the compensated camera images shows very clearly that the conventional models fail to fully hide the background, where it is particularly the background edges which are visible. It is our assertion that the pixel–level radiometric models, failing to consider spatial effects, are insufficient to attain a sufficient degree of correction.

The quantitative report of the RMSE (5.7), CIE2000 [57], and SSIM [62] metrics is shown in Table 5.1 for Fig. 5.5. It comes as no surprise that in essentially all cases the channel-independent Bimber method is inferior to the mixed-channel Yoshida method,

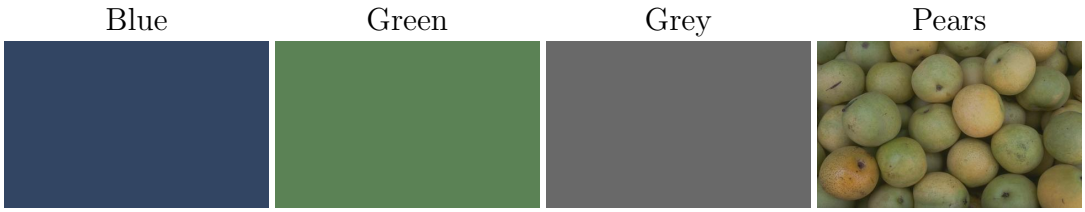

Figure 5.6: Target Images

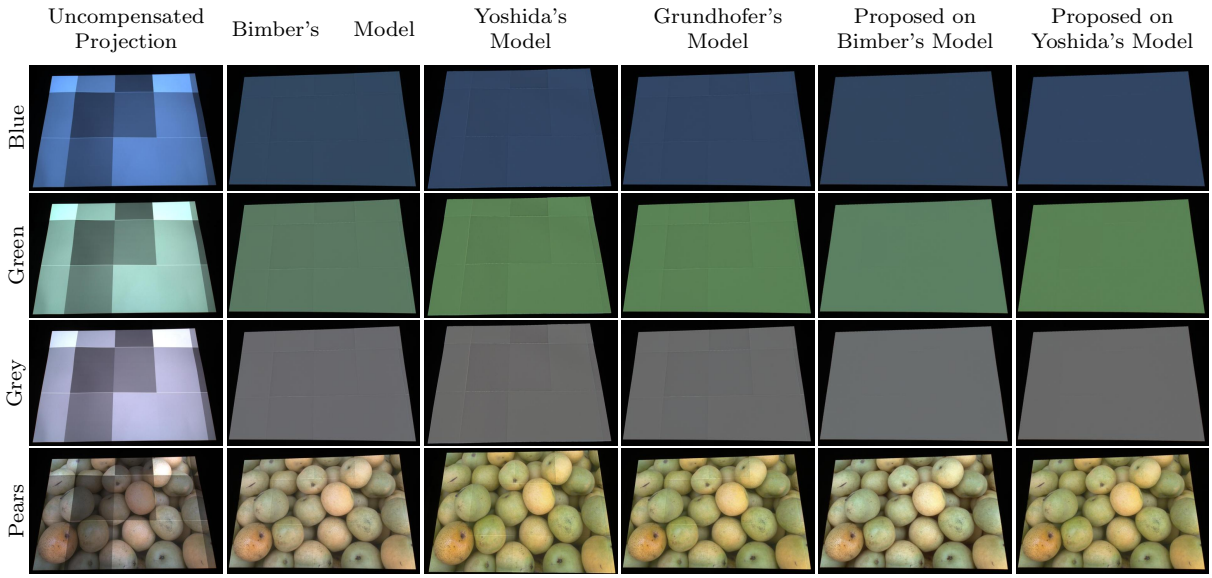

Figure 5.7: As in Fig. 5.5, the proposed approach is now applied to the background of Fig. 5.3a. The results are consistent with those of Fig. 5.5: the proposed approach significantly reduces background artifacts.

which itself performs less well than the non-linear approach of Grundhofer. It is gratifying that in every single case, for every image and every metric, the proposed approach applied to Yoshida's method offers the best result.

In practice, most radiometric compensation will involve the use of spatially *non*-uniform target images; that is, natural scenes, movies, Powerpoint presentations etc. To begin with, we select the standard *Pears* image as the target. As can be seen in Figs. 5.5 and 5.7, artifacts due to poor radiometric compensation tend to be masked by the variability and texture in the target image; nevertheless the same conclusion is reached, as is borne out in Table 5.1, that the proposed approach, although based on uniform target images, continues to outperform competing approaches for non-uniform targets. Table 5.1 lists results for both the *Pears* image on its own, and for a mixed set of 15 images, consisting of 7 uniform targets and 8 natural images.

A more detailed visualization of the performance of the proposed approach is illustrated in Fig. 5.8. Here, the RMSE and CIE2000 error maps have been plotted for all unsaturated pixels, with darker pixels indicating greater error values. From the error map, it can be observed that existing models give satisfactory performance in regions of uniform background contrast, but deviate from the target image in those regions of higher contrast. Grundhofer's model performs better than Yoshida's linear model. But the overall pattern of the error map is common for both methods. Although the proposed method still has errors present, as implied by darker pixels in the RMSE and CIE2000 maps, nevertheless there is nearly a complete absence of patterning due to the background.

5.2.5 Edge Error Metric

The proposed method cannot be claimed to universally improve RMSE or CIE2000 performance for all radiometric models; indeed, in Table 5.1 the proposed approach appears to *increase* the RMSE and CIE2000 metrics for Bimber's method, despite the fact that the visual results in Figs. 5.5 and 5.7 appear *significantly* improved with the proposed approach. The issue, we believe, is that the pixel–wise (i.e., point–wise) RMSE and CIE2000 metrics actually represent a poor measure of the human visual system, which is far more sensitive to spatially correlated edge-like artifacts. In response, we would propose a metric more aligned with the human visual system, based on differences of medians. That is, the human visual system is sensitive to systematic (correlated) differences, such as lines and edges, but less so to random noise. So we apply a median filter `med`() to distinguish between structure and noise, and then apply a differentiator. So given camera and target

images C, T, we find the RMSE metric

$$R_{ij} = \|C_{ij}, T_{ij}\| \tag{5.8}$$

and then apply differences to the median,

$$E = \left[G_x * \texttt{med}(R)\right]^2 + \left[G_y * \texttt{med}(R)\right]^2 \tag{5.9}$$

for Sobel kernels G_x, G_y and convolution operator $*$. The results of median filter on the error map is shown in Fig. 5.9. For a given image, the overall metric, reported in Table 5.2, is just the root-mean over the elements of E.

The results in Table 5.2 do, indeed, show that the proposed method produces improved results, for both channel-independent (Bimber) and channel-coupled (Yoshida) models, for every tested case.

Table 5.3 offers a comparison of the training and computational complexity of our proposed approach, applied to Yoshida's model, in comparison with other linear and non-linear models. Our proposed approach does require additional camera captures during calibration, because of the need to iteratively infer the inverse model. At a reasonable frame rate the total capture and learning time is still quite short, perhaps a few seconds. However our proposed approach continues to have the modest training data requirements and low number of parameters in common with the other linear models (Yoshida/Bimber), in contrast to Grudhofer's non-linear model.

5.3 Summary

In this chapter, two changes were proposed depending on the limitation of the existing radiometric compensation algorithms. The calibration set was modified to contain spatially uniform camera images and the compensation function is directly calculated from the calibration set. An iterative approach was used to form the proposed calibration set. The proposed approach can be applied to existing radiometric models to substantially increase their performance. The proposed changes were applied to the Bimber and Yoshida linear models and compared with Grundhofer's nonlinear model.

The application of the proposed inverse approach to Yoshida's linear model led to the best performance for every image and every metric tested, including performance superior to the non-linear model. Based on experimental results, the increased performance of the inverse model in hiding the background texture is striking, both in terms of image metrics

RMSE Edge Error

Image	Uncompensated	Bimber	Yoshida	Grundhofer	Proposed Bimber	Proposed Yoshida
Blue	230.11	10.59	7.94	4.26	3.96	0.81
Green	350.31	29.38	15.26	7.84	7.05	1.30
Grey	376.97	19.74	14.42	8.22	5.40	1.38
Pears	179.29	13.26	17.51	4.92	7.26	3.10
15 Images (Avg.)	297.54	19.73	14.22	6.35	6.22	1.74

CIE2000 Edge Error

Image	Uncompensated	Bimber	Yoshida	Grundhofer	Proposed Bimber	Proposed Yoshida
Blue	31.88	3.49	3.87	0.69	2.61	0.30
Green	139.53	21.44	3.83	2.41	3.82	0.31
Grey	61.89	9.99	2.68	3.09	2.79	1.15
Pears	53.81	11.75	5.57	1.62	5.56	0.77
15 Images (Avg.)	85.47	12.56	4.44	2.19	3.81	0.71

Table 5.2: Per the median metric illustrated in Fig. 5.9, median edge scores are tabulated as in Table 5.1. We now observe striking improvements for both Bimber's and Yoshida's methods in all cases.

and to the human eye. For both spatially uniform and non-uniform target images, the inverse model is able to produce perceptually superior compensated images.

The new framework helps in optimizing the calibration set to get the best performance from the radiometric compensation algorithms. By performing the iterative method for a selected few target images, we were able to get enchanced performance from the compensation models. Reducing the radiometric artifacts begins to highlight the saturation artifacts in the compensated images. Since the saturation artifacts are due to the projector

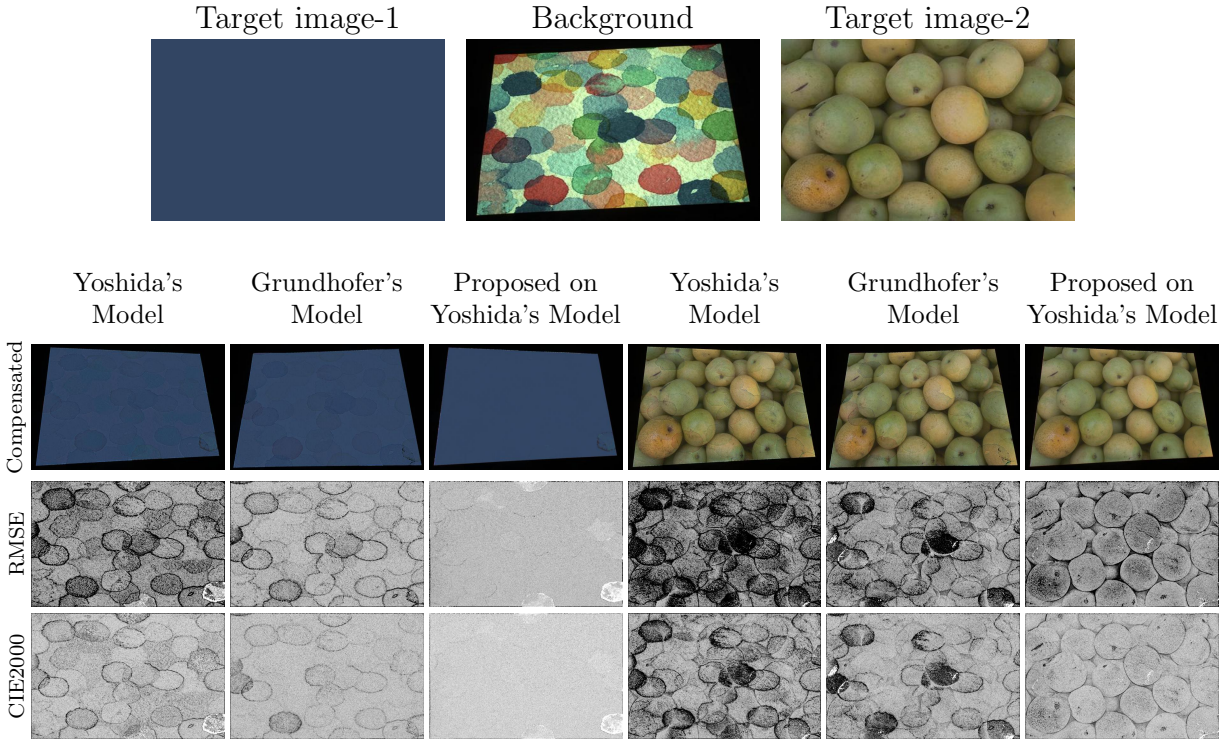

Figure 5.8: Error map comparison between Yoshida, Grunhofer and our proposed method. RMSE and CIE2000 error maps are shown in the second and third rows respectively. The RMSE error maps show the regions of absolute error and CIE2000 shows the error maps as perceived by the human eye.

Model	#Image Pairs (Q)	#Captures	#Parameters
Bimber	≈10	Q	6
Yoshida	≈10	Q	12
Grundhofer	≥125	Q	≥125
Proposed	≈10	10*Q	12

Table 5.3: Computational complexity comparison during calibration. With no increase in model complexity and a few additional camera captures, the proposed model is able to perform better than the non-linear model.

limitations, image enhancement techniques are used to reduce the perceptual sensitivity

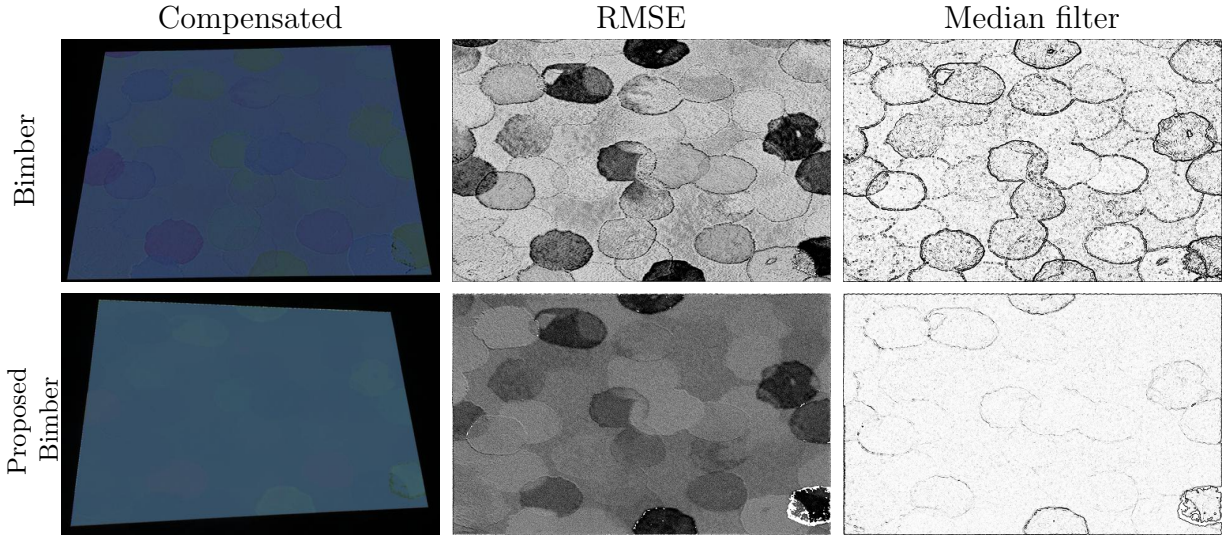

Figure 5.9: A more effective metric is needed which penalizes edge-like artifacts particularly visible to the eye. Rather than a metric such as RMSE, we propose median-filtered absolute-differences, such that smooth constant errors and random noise are ignored, but that correlated edge artifacts are amplified. The illustration here shows Bimber's method (top) and our proposed approach applied to Bimber's Model (bottom), such that our proposed approach makes the RMSE worse, but in fact the compensated image and the median metric are both improved.

of these unavoidable artifacts. The next chapter discusses the saturation artifacts and the corresponding artifact sensitivity reduction techniques in detail.

Chapter 6

Image Enhancement

6.1 Introduction

Radiometric compensation algorithms help in projecting a target image onto a textured background surface. Ideally, the algorithm should completely hide the background texture and achieve the desired image appearance on the surface. As described in Chapter 3, the exposure value of the camera controls the brightness of the compensated projector image, subsequently the perceived brightness of the projection. By increasing the exposure of the camera, the brightness of the projection is reduced and vice–versa.

For a fixed camera exposure, the achievable intensity on the background is limited by the background texture and the dynamic range of the projector. Since the texture vary arbitrarily from pixel to pixel, each projector pixel has a different range of achievable intensity on a given background. This constrains the range of target images which can be projected on the background without artifacts. For target image with pixel values outside the achievable range, the compensated projector image's pixel intensity is saturated, resulting in artifacts at the saturated regions.

Different image enhancement techniques are proposed in the literature [5, 50, 30, 26, 60] to fit the target image inside the achievable range without noticeable change to the original image. The popular approach is to use human visual system properties [26, 60] to modify the target image so that the saturation artifacts are reduced with minimum perceivable change. The revised target image is then given as input to the radiometric compensation algorithms for projection. The flowchart of the general framework is shown in Fig. 6.1. In this chapter, we examine the framework in detail and propose a novel spatially masked luminance modification model to reduce saturation artifacts.

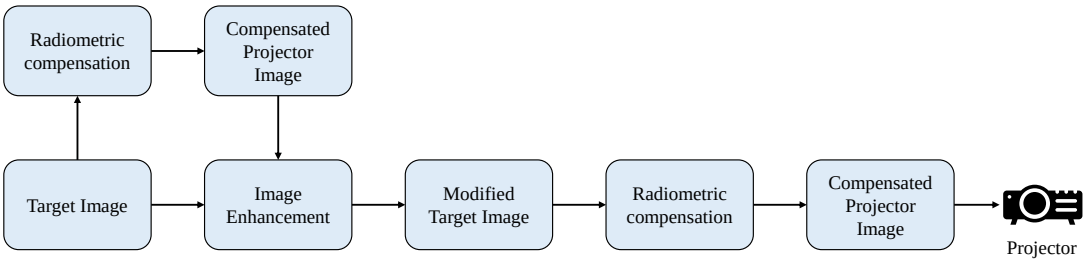

Figure 6.1: Flowchart of the image enhancement technique. Radiometric compensation is used twice: To calculate the initial saturation error and to calculate the final compensated image for projection.

6.2 Saturation Artifacts

The dynamic range of the projector defines the maximum and minimum intensity values in each channel of the imaging device. For a given projector–camera setup, the compensated projector image P_c values, obtained from the compensation algorithm, can go beyond the dynamic range of the projector. Since the projector is not capable of projecting the compensated image P_c, it instead projects a saturated image P_{sc} given by

$$P_{sc}(x,y,c) = \begin{cases} P_c(x,y,c), & \text{if } P_{\min} < P_c(x,y,c) < P_{\max} \\ P_{\min}, & \text{if } P_c(x,y,c) < P_{\min} \\ P_{\max}, & \text{if } P_{\max} < P_c(x,y,c) \end{cases} \tag{6.1}$$

$P_{\max}$ and $P_{\min}$ define the maximum and minimum limits of the projector. c indicates the projector's channel. Typically, the modern projectors come with $P_{\max} = 255$ and $P_{\min} = 0$. The limitations on the maximum and minimum value create two types of saturation. The upper saturation at pixel (x, y) for channel c occurs when $P_c(x, y, c) > P_{\max}$. The resultant error can be interpreted as the inability of the projector to mask the background texture resulting in artifacts. Lower saturation happens when $P_c(x, y, c) < P_{\min}$, is caused due to the presence of environmental light and projector offset.

Fig. 6.2 shows the results of Yoshida's linear model. The results are simulated to achieve ideal radiometric compensation, leaving only saturation artifacts in the compensated camera image C_c. The regions of upper and lower saturation are shown in Fig. 6.3a & 6.3b respectively, where the color at the pixel represents the saturated channel. We can observe that the saturation of one or two channels distort the chrominance of P_c, leading to visible artifacts at the compensated camera image C_c.

The most popular approach to reduce saturation artifacts is to modify the luminance of the target image, such that the new compensated projector image values fits inside the projector gamut. For a saturated pixel, modifying the luminance of the pixel will alter the brightness demands of the projector, resulting in reduced chrominance distortion at the P_{sc}. As luminance distortions are much less sensitive than chrominance distortion, target image modification results in perceptually improved compensated images.

Luminance alteration to the target image reduces the saturation error by introducing image modification error. Image enhancement techniques are developed to optimize this trade-off between saturation and modification error. The optimization results in the reduction of undesired saturation error by introducing visually pleasing and less sensitive luminance modification errors. The human visual system properties [56, 9] can be used to find less perceivable modifications that reduce the saturation error. Wang *et al.*[60] and Grundhofer *et al.*[26] used threshold map constructed using human visual system properties to calculate the optimum local and global luminance changes.

We start the next section by exploring the saturation artifacts. A local luminance modification method is suggested to reduce the saturation. A novel spatial modification framework is proposed to reduce the perceptual sensitivity of the local luminance modification.

6.3 Artifact Sensitivity

In this section, we explore the framework where human visual system properties can be used to reduce the saturation artifact. In particular, we know that abrupt changes in image luminance are more sensitive to human visual system [56, 9] than gradual change in luminance. We also understand that luminance manipulation is perceptually less sensitive and can be masked by the contrast of the image [12]. Using these two properties, the proposed framework first modifies the luminance at the saturation regions. The sensitivity of the luminance modification is then reduced using spatial correction by adjusting abrupt changes to have continuous variation. The proposed framework can be divided into three modules:

- Identifying the saturated regions;
- Pixel–wise luminance modification;
- Spatial correction to reduce the modified luminance's perceptual sensitivity,

The framework can be combined with any radiometric compensation algorithm to reduce saturation artifacts. The following subsections examine each module in detail.

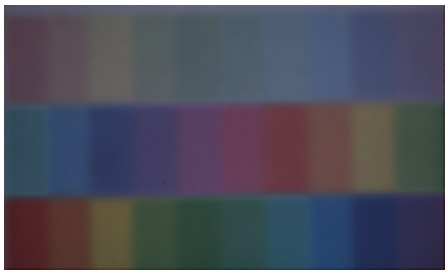

(a) Projector screen

(b) Target image

(c) Compensated Projector image

(d) Compensated camera image

Figure 6.2: Results of simulated compensation by Yoshida's linear model[64]. Due to the limited dynamic range of the projector, one or more channels of the compensated projector image are saturated resulting in chrominance artifacts in the final compensated image.

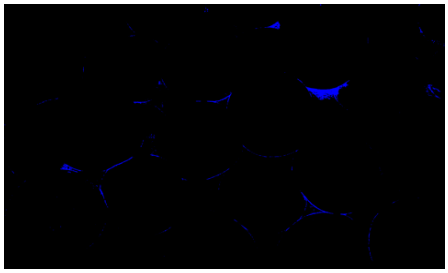

(a) Upper Saturation

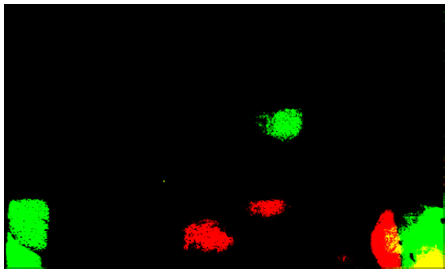

(b) Lower Saturation

Figure 6.3: Saturated regions of the Yoshida's linear model from Fig. 6.2. The saturated pixels are highlighted for (a) upper saturation and (b) lower saturation. The color of the pixel indicates the saturated channels.

6.3.1 Saturated Regions

In order to find the saturated regions, the proposed framework requires the radiometric compensation algorithm to calculate the compensated projector image P_c for the unmodified target image T. A pixel is considered saturated if the intensity of one or more channels goes beyond the dynamic range of the projector. Assuming a modern RGB projector takes values between $P_{\min}$ and $P_{\max}$, upper saturation occurs when at least one channel value goes beyond $P_{\max}$, similarly lower saturation happens when the value goes below $P_{\min}$. It is also possible for a pixel to have upper saturation at one channel and lower saturation at another. Upper and lower saturation maps which highlight the corresponding saturated pixels can be constructed as shown in Fig. 6.4e and Fig. 6.4b respectively.

From the results of the Yoshida's linear model, as shown in Fig. 6.2, we can observe that the structured saturation artifact are prominent to the human visual system. Artifacts from randomly distributed saturated pixels are hardly visible to the observer. These random artifacts are masked by the content and texture complexity of the image. To avoid unnecessary alteration to the target image, a median filter is applied to the saturation map to ignore random saturated pixels. The size of the median filter can be modified depending on the required degree of tolerance.

Fig. 6.4 shows the impact of median filter on the saturation map. The median filter helps us to ignore the random saturation artifacts which are less sensitive to the human visual system. In our experiments we used a 11×11 filter. The luminance changes are applied to the median filtered pixels as defined in the following subsection.

6.3.2 Pixel–Wise Correction

Luminance manipulation is carried out on the saturated pixels returned by the median filter. In our case, we have defined the luminance of a RGB image I as

$$L(x, y) = \frac{I(x, y, 1) + I(x, y, 2) + I(x, y, 3)}{3} \tag{6.2}$$

By giving equal importance to each channel, the luminance manipulation is equally distributed among all the channels of the projector. As discussed in Section 6.2, the upper saturation is caused due to the projector's limited brightness. So reducing the luminance of the target image should reduce the required intensity demand from the projector. So for upper saturation pixels, the modified target image value $T_m(x, y)$ is defined as

$$T_m(x, y) = \alpha_u(x, y) \cdot T(x, y) \tag{6.3}$$

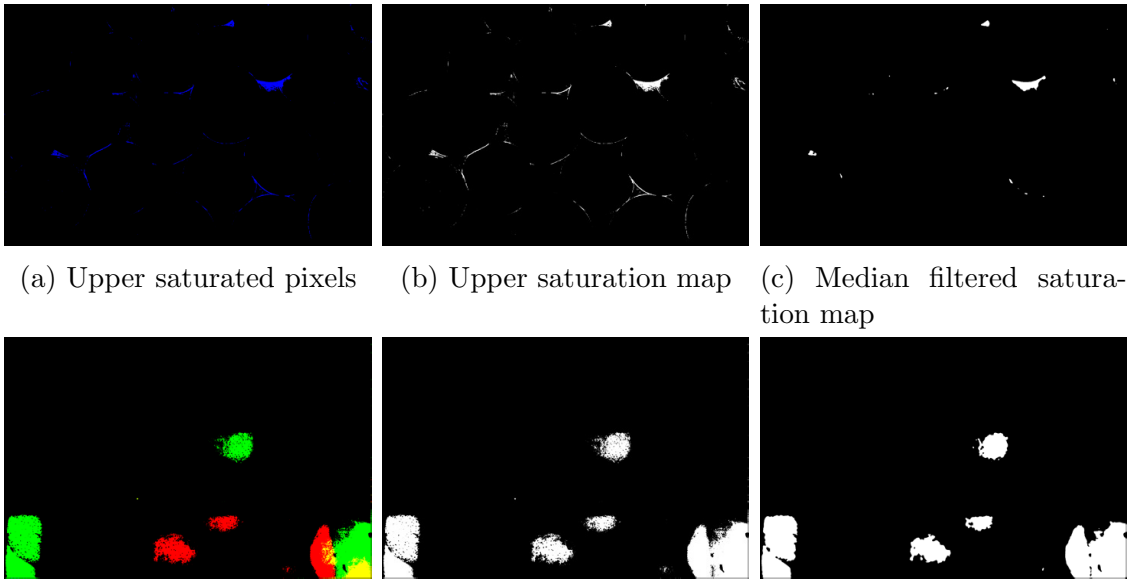

(a) Upper saturated pixels (b) Upper saturation map (c) Median filtered saturation map

(d) Lower saturated pixels (e) Lower saturation map (f) Median filtered saturation map

Figure 6.4: Result of median filter on the saturated map: un-structured random saturated pixels which are not prominent in a complex textured image are omitted by the median filter to avoid unwanted modifications to the target image.

The α_u value is calculated to achieve maximum luminance without saturation at a given pixel. It depends on the compensated projector image and background characteristics. The lower saturation is caused due to projector offset and environment light as the camera will capture non-zero intensity value for a zero projector pixel intensity. This causes the radiometric compensation algorithm to calculate negative projector intensity to achieve near-zero target image values. The lower saturation is also caused due to the background texture, where it is impossible to attain pure red on a pure green background. Since the saturation is due to low luminance or high contrast demands, the desired change should try to increase the luminance and reduce the contrast of the target image. So the modified target image is obtained by simultaneously reducing the contrast and increasing the brightness. The modified target image T_m at lower saturation pixels is given by

$$T_m(x,y) = \vec{P}_{\max} + (T(x,y) - \vec{P}_{\max}) \cdot \alpha_l(x,y) \tag{6.4}$$

$$\vec{P}_{\max} = \begin{bmatrix} P_{\max} & P_{\max} & P_{\max} \end{bmatrix}' \tag{6.5}$$

Here, as the α_l is reduced from 1 to 0, the target image contrast is reduced and brightness is increased from T to $\vec{P_{\max}}$. The α_u and α_l are calculated with respect to the radiometric compensation algorithm f_c. The maximum values of α_u and α_l which satisfies the following equations are used for target image modification

$$\vec{P}_{\min} < f_c\big(\vec{P}_{\max} + (T(x,y) - \vec{P}_{\max}) \cdot \alpha_l(x,y)\big) \tag{6.6}$$

$$f_c(\alpha_u(x,y) \cdot T(x,y)) < \vec{P}_{\max} \tag{6.7}$$

The maximum values are taken to ensure minimum change to the target image. For experiments, we have used Yoshida's linear model described in Section 2.4.1 as radiometric compensation algorithm. For a target image T, the compensated projector image P_c is calculated as

$$P_c = f_c(T) = V^{-1}(T - K) \tag{6.8}$$

V and K are the parameters of the Yoshida's linear model from Eqn. 2.10. For an upper saturation pixel (x,y), which is saturated at channel c, the maximized α_u value is given by

$$\alpha_u(x,y) = \frac{P_{\max} + V_k(c)}{P_c(x,y,c) + V_k(c)} \tag{6.9}$$

$$V_k = V(x,y)^{-1} \cdot K \tag{6.10}$$

Similarly for a lower saturation pixel, which is saturated at channel c, the maximized α_l value is given by

$$\alpha_l(x,y) = \frac{P_{\min} + V_k(c) - V_s(c)}{P_c(x,y) + V_k(c) - V_s(c)} \tag{6.11}$$

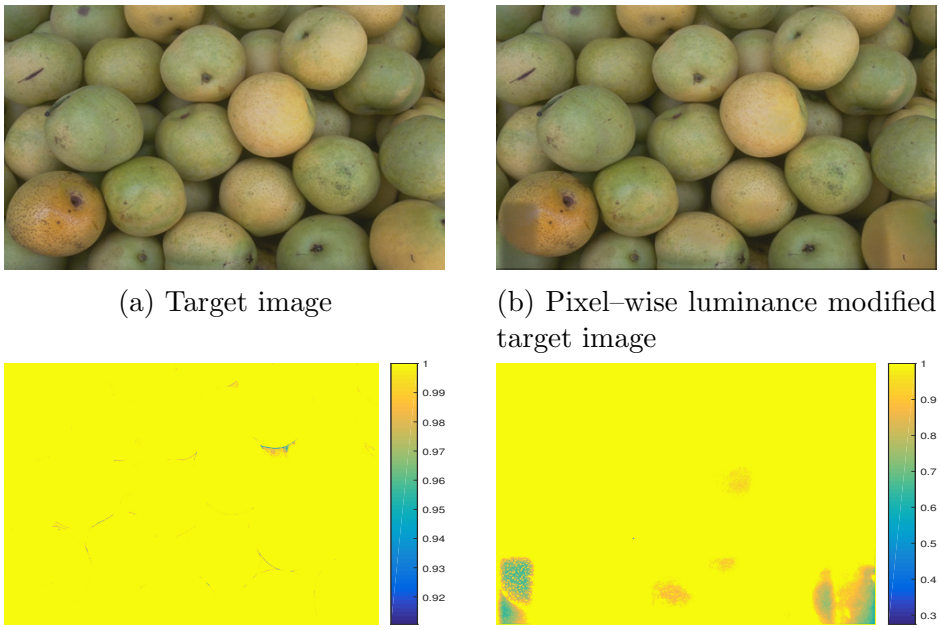

(a) Target image

(b) Pixel–wise luminance modified target image

(c) α_l image

(d) α_u image

Figure 6.5: The result of (b) pixel–wise luminance modification on the (a) target image at the saturated regions shown in Fig 6.4. The luminance modification is obtained by calculating the (c) α_l and (d) α_u map for the saturated regions and applying the proposed transformation. The luminance modification reduces the chrominance error at the saturated regions, but abrupt change in luminance creates artifacts in the modified target image.

$$V_s = V(x, y)^{-1} \cdot \vec{P}_{\max} \tag{6.12}$$

The results of pixel–wise luminance correction is shown in Fig. 6.5.

6.3.3 Spatial Correction

Pixel–wise luminance correction helps to avoid saturation artifacts and chrominance distortions. But an abrupt change in luminance creates artifacts in the compensated camera image. Since the human visual system is sensitive to these changes, a spatial modification is needed to form a gradual luminance change across the image that reduces the perceptual sensitivity of the artifacts. For each saturated pixel, the surrounding pixel's luminance is reduced and the amount of luminance reduction is inversely proportional to the distance

from the saturated pixel. Reducing the luminance of the surrounding pixels also decreases the overall brightness of the target image. This creates a trade-off between overall brightness and artifact sensitivity.

For a saturated pixel, α indicates the degree of luminance change, as α is increased towards 1, the change in the target image is continuously reduced. Here, α is used to indicate both α_u and α_l. To have a spatially smooth luminance change, a kernel is created for every saturated pixel which represents the luminance change for the surrounding pixels. For every saturated pixel, a linear kernel $k(x, y)$ can be created from the α value, as given by

$$k(x, y) = \alpha + s \cdot \sqrt{x^2 + y^2}, \tag{6.13}$$

A Gaussian kernel can also be created, where the rate of α change follows a Gaussian distribution as follows,

$$k(x, y) = 1 - (1 - \alpha)e^{-(x^2+y^2)/2\sigma^2} \tag{6.14}$$

where, σ is given by,

$$\sigma = \frac{1 - \alpha}{3 \cdot s} \tag{6.15}$$

The spatial extent for both kernels is defined for a range of x and y given by

$$x, y \in \left[-\frac{1 - \alpha}{s \cdot \sqrt{2}}, \frac{1 - \alpha}{s \cdot \sqrt{2}} \right] \tag{6.16}$$

The spatial extent and σ is determined such that the kernel values reaches towards 1 at the borders, indicating no further changes. After building a kernel for each saturated pixel, a β map is formed by combining all the kernels from the saturated pixels. It is constructed by placing the center of the kernel at their corresponding saturated pixel location and replacing the β maps value with kernel values. In the case of overlapping kernels, the minimum value from all the overlapping kernels was selected as the final β map's value. The minimum value is selected to ensure the least saturation. For unaffected pixels, the β map takes default value as 1. Two beta maps are obtained from α_u and α_l maps. Fig. 6.6 shows an example of the β_u and β_p map for different slope values. The final modified target image is obtained as given by:

$$T_{M1}(x, y) = P'_{\max} + \beta_0(x, y) \cdot (P'_{\max} - T(x, y)) \tag{6.17}$$

$$T_M(x, y) = \beta_1(x, y) \cdot T_{M1}(x, y) \tag{6.18}$$

Here, the lower saturation correction is followed by the upper saturation. The order of the saturation correction will not impact the performance of the algorithm. The results of the spatial correction for different values of slope are shown in Fig. 6.6.

(a) slope = 0.0120 (b) slope = 0.0024 (c) slope = 0.0006

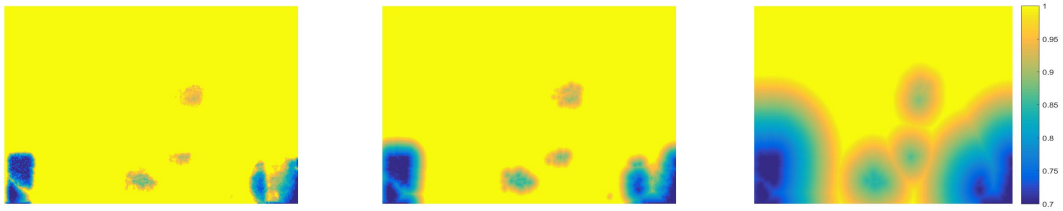

(d) β_u map (e) β_u map (f) β_u map

(g) β_l map (h) β_l map (i) β_l map

Figure 6.6: The first row shows the results of spatial modification for different values of slope s. As the slope is reduced, the luminance change is spread over a wider region, reducing the sensitivity of the modification. However, the overall brightness of the image is also reduced. The second and third rows show the corresponding β_u and β_l map respectively.

6.4 Experiments & Results

The projector–camera system is formed as suggested in Chapter 3. The system was linearized and gray scale coding was used to form the pixel correspondence. Yoshida's linear model was used as the radiometric compensation algorithm. The calibration set was formed as suggested in [64]. The color mixing matrix V and K are calculated from the calibration set for each projector–camera pixel pair. For target image T, the compensated projector image P_c was calculated as shown in (6.4). Since the P_c values are saturated by the projector, P_{sc} from (6.1) is projected and captured by the camera to form the compensated camera image C_c. But, C_c can't be evaluated for saturation artifacts due to the presence of radiometric artifacts. It is impossible to separate the saturation artifacts from the overall error in a camera captured C_c. But the camera image can be simulated to attain an ideal compensation removing radiometric artifacts. Instead of projecting P_c and capturing C_c, the simulated compensation image S_c is obtained by

$$S_c = VP_{sc} + K \tag{6.19}$$

S_c contains only the saturated artifacts without radiometric artifacts. The deviation of S_c from T is examined to understand the saturation artifacts. In this chapter, the compensated images are obtained through simulation.

First, pixel–wise luminance modification was carried out as mentioned in Section 6.3.2. In order to avoid massive alteration to the target image, the α_u and α_l values were limited between $\alpha_{\min}$ to 1. The $\alpha_{\min}$ value is chosen, depending on the tolerated luminance modification. All of the calculated values outside the range are replaced by their corresponding limits. Varying the $\alpha_{\min}$ helps in controlling the degree of luminance correction tolerated in the compensated image. In our experiments we found $\alpha_{\min} = 0.7$ to be an optimum tolerance value for the given viewing condition. After pixel–wise luminance correction, the proposed spatial modification is performed around saturated pixels. A linear and Gaussian kernel is explored for spatial modifications. For a fixed spatial extent s, Fig. 6.7 compares the results of the compensation by two kernels. We can observe that the linear kernel is resulting in a more visually pleasing luminance change than the Gaussian kernel.

The slope value s can be configured depending on the required trade-off between overall brightness and the saturation artifacts. The simulated images for different slope values are shown in Fig. 6.6. We can observe that as the slope becomes steeper, the luminance change seems more noticeable. As expected, steeper slope also lead to minimum brightness reduction. Experimentally $s = 0.0006$ was found to have a good trade-off between brightness and artifacts sensitivity.

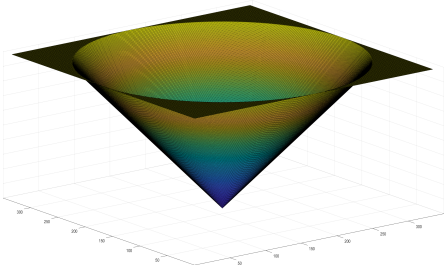

(a) Linear kernel

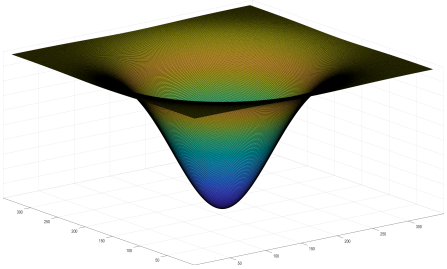

(b) Gaussian kernel

(c) Linear kernel based spatial modification

(d) Gaussian kernel based spatial modification

Figure 6.7: Results of spatial modification based on linear and Gaussian kernel is compared. For the same spatial extent, linear kernels produce perceptually less sensitive luminance modification.

The results of the proposed spatial modification with linear kernel and slope $s = 0.0006$ is compared with the global and pixel–wise correction in Fig. 6.9. Global luminance reduction is done by multiplying the target image by a single factor. Similar to spatial luminance correction, the global luminance correction is carried out as follows,

$$T_{G1} = P'_{\max} + \min(\beta_0) \cdot (P'_{\max} - T(x, y)) \tag{6.20}$$

$$T_{GM} = \min(\beta_1) \cdot T_{G1}(x, y) \tag{6.21}$$

Minimum values of β_1 and β_0 maps are considered for global correction. Here, global luminance change can be imagined as an brightness sacrifice across all pixels for zero artifact sensitivity, whereas pixel–wise luminance change maintains maximum achievable luminance without any artifact sensitivity reduction. The proposed framework achieves a trade-off between the luminance and artifacts by localized spatial correction around the saturation artifacts. From the results, we can observe that the proposed spatial modification is almost always visually more pleasing than the global or pixel–wise luminance change. The spatially modified simulated image is also significantly closer to the target image than the compensated camera image.

6.5 Summary

In this chapter, saturation artifacts due to the limited dynamic range of the projector are discussed in detail. Two types of saturation encountered due to the upper and lower limit of the projector gamut are examined. Luminance modification, inspired from human visual system properties, is suggested as a solution to the saturation artifacts. Pixel–wise luminance modification was proposed which can be used with any radiometric compensation algorithm to reduce saturation. Yoshida's linear model was used as an example to elaborate the working of the pixel–wise correction model. To further reduce the sensitivity of the luminance modification, a novel spatial modification was proposed to create smooth luminance variation across the image making the artifact less sensitive to the human visual system. Different kernels were explored to understand the nature of the spatial modification. The parameter s, which determines the degree of smoothness was optimized for the trade-off between image luminance and artifact sensitivity. Simulated results of the proposed model were compared with the global and pixel–wise correction to verify the improvement in performance.

Figure 6.8: Target images

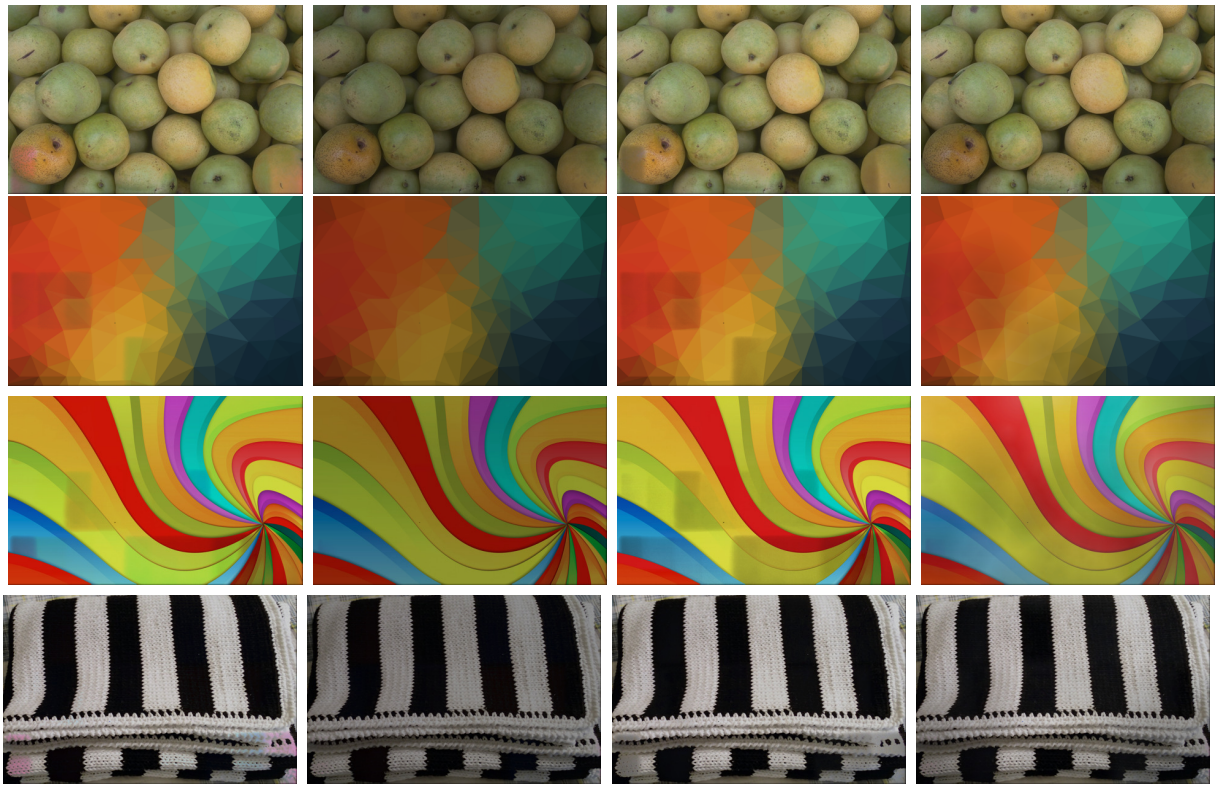

(a) Compensated image with saturation.

(b) Global Correction

(c) Pixel–wise Correction

(d) Proposed Spatial Correction

Figure 6.9: The simulated results of the proposed spatial correction is compared with the results of global, pixel–wise luminance modified target images. The proposed method is able to produce perceptually pleasing images similar to the target images. The luminance change is able to reduce the chrominance error and localized spatial modification is able to reduce the sensitivity of luminance change.

Chapter 7

Conclusion

7.1 Summary

In this thesis, different components of the projector compensation framework were discussed and radiometric compensation was examined in detail. Various assumptions associated with the existing radiometric models were studied and their performance on the background with sharp edges was examined. It was found that the pixel level radiometric model's performance was affected by the choice of projector image in the calibration set and led to background edge artifacts in the compensated image. A novel framework was proposed that optimized the calibration set used for model development. The proposed calibration set contains smooth camera images and its corresponding non-uniform projector images. The smooth camera images were obtained using an iterative approach. The new framework also suggested to directly learn the compensation model from the calibration set instead of inverting the learned radiometric model. Due to the inter–pixel coupling, the compensation model is not equivalent to the inverse of the radiometric model and directly finding the compensation model from the calibration set produces the best estimate of the required model.

The proposed framework applied to Yoshida's and Bimber's linear models was able to hide the background's texture and edges completely. Its performance was compared with the state of the art non-linear model using RMSE, SSIM and CIE2000 error metrics. A novel median–based edge error metric was used to compare the ability of the radiometric models to hide the background edges. The proposed method applied to Yoshida's linear model was able to achieve the best performance among the existing linear and non–linear models. The optimum performance was achieved without any increase in model complex-

ity. The proposed approach can be combined with any radiometric model to improve its performance and robustness.

In Chapter 6, two types of saturation artifacts encountered during radiometric compensation were studied. Pixel–wise luminance correction was proposed to reduce the chrominance distortion at the saturated regions. To further reduce the perceptual sensitivity of the luminance correction, a novel spatial luminance modification method was proposed to have gradual luminance variation across the image. The simulated results of pixel–wise correction and spatially optimized correction were compared with the global luminance correction method to show the superiority of the proposed approach. The approach enables the use of limited dynamic range projectors for radiometric compensation by modifying the target image with respect to the projector gamut.

The inverse approach can be combined with the spatial modification to provide a robust projector compensation framework, which can optimize projection on any arbitrary background surface using any projector. The inverse approach can be used separately on existing radiometric compensation model to improve its performance. Similarly, the spatial modification can be combined with existing radiometric compensation models to reduce saturation artifacts.

7.2 Future Work

The approaches proposed in this thesis can improve the performance of the existing models. However, this research can further be extended. For radiometric compensation, the following extensions can be made:

- The brightness leakage of the projector–camera system can be modelled and incorporated into the compensation function to completely hide the edge artifacts for smooth and textured target images.
- The compensation model can be developed such that the corrections are made with respect to the human visual system, instead of the camera intensity values.
- The pixel based model can be made more efficient by analyzing the background surface and clustering pixels with similar properties to develop a faster compensation model.

The proposed image enhancement technique can also be improved by working on the following:

- Temporal adaptation of the luminance adjustment is needed to apply the spatial modification approach to videos.
- Image quality assessment based on the human visual system's luminance and contrast sensitivity can be applied to evaluate the performance of the proposed model.
- A successful human visual system based error metric can lead the way for an optimization framework which can automatically estimate the optimum slope s and α_{min} described in Sections 6.3 & 6.4.
- Human visual system properties can also be used to chose different spatial extent or slope value s for each saturated pixel depending on the luminance and contrast of the surrounding regions, instead of constant slope s for an entire image as described in Section 6.3.

Future steps provide different ways in which the projector compensation can further be improved to make ubiquitous use of projectors on any background surface a reality.

References

[1] Windows 7 calibrating your monitor's color. In *Bob Cerelli's Windows page*, January, 2009. http://www.onecomputerguy.com/windows7/windows7_calibrate_color.htm.

[2] Imaging electronics 101: Basics of digital camera settings for improved imaging results. In *Edmund Optics*, November, 2011. https://www.edmundoptics.com/resources/application-notes/imaging/basics-of-digital-camera-settings-for-improved-imaging-results/.

[3] White balance. In *Nikon Digital*, October, 2016. http://...http://www.nikondigital.org/articles/white_balance.htm.

[4] Cecilia Aguerrebere, Andrés Almansa, Yann Gousseau, Julie Delon, and Pablo Muse. Single shot high dynamic range imaging using piecewise linear estimators. In *IEEE International Conference on Computational Photography (ICCP)*, pages 1–10. IEEE, 2014.

[5] Mark Ashdown, Takahiro Okabe, Imari Sato, and Yoichi Sato. Robust content-dependent photometric projector compensation. In *Computer Vision and Pattern Recognition Workshop, 2006. CVPRW'06. Conference on*, pages 6–6. IEEE, 2006.

[6] Dirk Bergmann. New approach for automatic surface reconstruction with coded light. In *International Symposium on Optical Science, Engineering, and Instrumentation*, pages 2–9. International Society for Optics and Photonics, 1995.

[7] Oliver Bimber, Andreas Emmerling, and Thomas Klemmer. Embedded entertainment with smart projectors. In *Computer*, volume 38.1, pages 48–55. IEEE, 2005.

[8] Panagiotis-Alexandros Bokaris, Michèle Gouiffès, Christian Jacquemin, Jean-Marc Chomaz, and Alain Trémeau. One-frame delay for dynamic photometric compensation

in a projector-camera system. In *Image Processing (ICIP), 2015 IEEE International Conference on*, pages 2675–2679. IEEE, 2015.

[9] David C Burr, M Concetta Morrone, and Donatella Spinelli. Evidence for edge and bar detectors in human vision. In *Vision research*, volume 29, pages 419–431. Elsevier, 1989.

[10] Xinli Chen, Xubo Yang, Shuangjiu Xiao, and Meng Li. Color mixing property of a projector-camera system. In *Proceedings of the 5th ACM/IEEE International Workshop on Projector camera systems*, page 14. ACM, 2008.

[11] Po-Jung Chiu and Shao-Yi Chien. Painted face effect removal by a projector-camera system with dynamic ambient light adaptability. In *International Conference on Multimedia and Expo (ICME)*, pages 1–6. IEEE, 2015.

[12] Karen K De Valois and Eugene Switkes. Simultaneous masking interactions between chromatic and luminance gratings. In *JOSA*, volume 73, pages 11–18. Optical Society of America, 1983.

[13] Paul E Debevec and Jitendra Malik. Recovering high dynamic range radiance maps from photographs. In *Proceedings of the 24th annual conference on Computer graphics and interactive techniques*, pages 369–378. ACM Press/Addison-Wesley Publishing Co., 1997.

[14] Gianluca Donato and Serge Belongie. Approximate thin plate spline mappings. In *European Conference on Computer Vision*, pages 21–31. Springer, 2002.

[15] Jean Duchon. Splines minimizing rotation-invariant semi-norms in Sobolev spaces. In *Constructive Theory of Functions of Several Variables*, pages 85–100. Springer, 1977.

[16] Chen Feng and Liu Yue. Radiometric compensation techniques based on projector-camera system. In *Journal of Computer-Aided Design & Computer Graphics*, volume 6, page 005, 2015.

[17] Mark Freeman, Mark Champion, and Sid Madhavan. Scanned laser pico-projectors: seeing the big picture (with a small device). In *Optics and photonics news*, volume 20, pages 28–34. Optical Society of America, 2009.

[18] Kensaku Fujii, Michael D Grossberg, and Shree K Nayar. A projector-camera system with real-time photometric adaptation for dynamic environments. In *IEEE Computer Society Conference on Computer Vision and Pattern Recognition*, volume 1, pages 814–821. IEEE, 2005.

[19] Alan Gilchrist, Christos Kossyfidis, Frederick Bonato, Tiziano Agostini, Joseph Cataliotti, Xiaojun Li, Branka Spehar, Vidal Annan, and Elias Economou. An anchoring theory of lightness perception. In *Psychological review*, volume 106, page 795. American Psychological Association, 1999.

[20] Rafael C Gonzalez, Richard E Woods, Steven L Eddins, et al. Digital image processing using matlab. volume 624. Pearson-Prentice-Hall Upper Saddle River, New Jersey, 2004.

[21] Michael D Grossberg and Shree K Nayar. What can be known about the radiometric response from images? In *European conference on computer vision*, pages 189–205. Springer, 2002.

[22] Michael D Grossberg and Shree K Nayar. Determining the camera response from images: What is knowable? In *IEEE Transactions on Pattern Analysis & Machine Intelligence*, number 11, pages 1455–1467. IEEE, 2003.

[23] Michael D Grossberg and Shree K Nayar. What is the space of camera response functions? In *Computer Vision and Pattern Recognition, 2003. Proceedings. 2003 IEEE Computer Society Conference on*, volume 2, pages II–602. IEEE, 2003.

[24] Michael D Grossberg and Shree K Nayar. Modeling the space of camera response functions. In *IEEE transactions on pattern analysis and machine intelligence*, volume 26, pages 1272–1282. IEEE, 2004.

[25] Michael D Grossberg, Harish Peri, Shree K Nayar, and Peter N Belhumeur. Making one object look like another: Controlling appearance using a projector-camera system. In *Proceedings of the 2004 IEEE Computer Society Conference on Computer Vision and Pattern Recognition*, volume 1, pages I–I. IEEE, 2004.

[26] A. Grundhofer and O. Bimber. Real-time adaptive radiometric compensation. In *IEEE Transactions on Visualization and Computer Graphics*, volume 14.1, pages 97–108, Jan 2008.

[27] Anselm Grundhöfer. Practical non-linear photometric projector compensation. In *Proceedings of the IEEE Conference on Computer Vision and Pattern Recognition Workshops*, pages 924–929, 2013.

[28] Anselm Grundhöfer and Daisuke Iwai. Robust, error-tolerant photometric projector compensation. In *IEEE Transactions on Image Processing*, volume 24.12, pages 5086–5099. IEEE, 2015.

[29] Tai-Hsiang Huang, Chen-Tai Kao, and Homer H Chen. Quality enhancement of pro-cam system by radiometric compensation. In *Multimedia Signal Processing (MMSP), 2012 IEEE 14th International Workshop on*, pages 192–197. IEEE, 2012.

[30] Tai-Hsiang Huang, Ting-Chun Wang, and Homer H Chen. Radiometric compensation of images projected on non-white surfaces by exploiting chromatic adaptation and perceptual anchoring. In *IEEE Transactions on Image Processing*, volume 26, pages 147–159. IEEE, 2017.

[31] Seiji Inokuchi. Range-imaging system for 3D object recognition. In *Proc. of 7th International Conference on Pattern Recognition*, 1984.

[32] Anil K Jain. Fundamentals of digital image processing. 1989. In *The Back-Projection Operator*, volume 445.

[33] Seon Joo Kim, Hai Ting Lin, Zheng Lu, Sabine Süsstrunk, Stephen Lin, and Michael S Brown. A new in-camera imaging model for color computer vision and its application. In *IEEE Transactions on Pattern Analysis and Machine Intelligence*, volume 34.12, pages 2289–2302. IEEE, 2012.

[34] Hsien-Che Lee. Introduction to color imaging science. Cambridge University Press, 2005.

[35] Joon-Young Lee, Yasuyuki Matsushita, Boxin Shi, In So Kweon, and Katsushi Ikeuchi. Radiometric calibration by rank minimization. In *IEEE transactions on pattern analysis and machine intelligence*, volume 35, pages 144–156. IEEE, 2013.

[36] Moon-Hyun Lee, Hanhoon Park, and Jong-Il Park. Fast radiometric compensation accomplished by eliminating color mixing between projector and camera. In *IEEE Transactions on Consumer Electronics*, volume 54. IEEE, 2008.

[37] Yuqi Li, Aditi Majumder, Meenakshisundaram Gopi, Chong Wang, and Jieyu Zhao. Practical radiometric compensation for projection display on textured surfaces using a multidimensional model. In *Computer Graphics Forum*, volume 37, pages 365–375. Wiley Online Library, 2018.

[38] Stephen Lin and Lei Zhang. Determining the radiometric response function from a single grayscale image. In *Computer Vision and Pattern Recognition, 2005. CVPR 2005. IEEE Computer Society Conference on*, volume 2, pages 66–73. IEEE, 2005.

[39] Hongyu Liu, Wei-Hung Su, Karl Reichard, and Shizhuo Yin. Calibration-based phase-shifting projected fringe profilometry for accurate absolute 3D surface profile measurement. In *Optics communications*, volume 216, pages 65–80. Elsevier, 2003.

[40] Jen-Shuo Liu and Homer H Chen. Preserving image color appearance on non-white projection surfaces. In *International Conference on Multimedia and Expo Workshops (ICMEW)*, pages 1–6. IEEE, 2015.

[41] S Mann and R Picard. Beingundigital'with digital cameras. In *MIT Media Lab Perceptual*, volume 1, page 2, 1994.

[42] Yasuyuki Matsushita and Stephen Lin. Radiometric calibration from noise distributions. In *Computer Vision and Pattern Recognition, 2007. CVPR'07. IEEE Conference on*, pages 1–8. IEEE, 2007.

[43] Shoichiro Mihara, Daisuke Iwai, and Kosuke Sato. Artifact reduction in radiometric compensation of projector-camera systems for steep reflectance variations. In *IEEE Transactions on Circuits and Systems for Video Technology*, volume 24.9, pages 1631–1638. IEEE, 2014.

[44] Tomoo Mitsunaga and Shree K Nayar. Radiometric self calibration. In *CVPR*, page 1374. IEEE, 1999.

[45] Isao Miyagawa, Yoshiko Sugaya, Hiroyuki Arai, and Masashi Morimoto. An iterative compensation approach without linearization of projector responses for multiple-projector system. In *IEEE Trans. Image Processing*, volume 23, pages 2676–2687, 2014.

[46] Nathan Moroney, Mark D Fairchild, Robert WG Hunt, Changjun Li, M Ronnier Luo, and Todd Newman. The ciecam02 color appearance model. In *Color and Imaging Conference*, volume 2002, pages 23–27. Society for Imaging Science and Technology, 2002.

[47] Shree K Nayar, Harish Peri, Michael D Grossberg, and Peter N Belhumeur. A projection system with radiometric compensation for screen imperfections. In *ICCV workshop on Projector-Camera Systems (PROCAMS)*, volume 3. Citeseer, 2003.

[48] Hanhoon Park, Moon-Hyun Lee, Byung-Kuk Seo, Jong-Il Park, Moon-Sik Jeong, Tae-Suh Park, Yongbeom Lee, and Sang Ryong Kim. Simultaneous geometric and radiometric adaptation to dynamic surfaces with a mobile projector-camera system.

In *IEEE Transactions on Circuits and Systems for Video Technology*, volume 18, page 110. INSTITUTEOF ELECTRICAL AND ELECTRONICS ENGINEERS, 2008.

[49] Hanhoon Park, Moon-Hyun Lee, Byung-Kuk Seo, Hong-Chang Shin, and Jong-Il Park. Radiometrically-compensated projection onto non-lambertian surface using multiple overlapping projectors. In *Pacific-Rim Symposium on Image and Video Technology*, pages 534–544. Springer, 2006.

[50] Sun Hee Park, Sejung Yang, and Byung-Uk Lee. Adaptive chrominance correction for a projector considering image and screen color. In *International Symposium on Visual Computing*, pages 751–759. Springer, 2007.

[51] Charles Poynton. Digital video and HD: Algorithms and interfaces. Elsevier, 2012.

[52] Mahesh Ramasubramanian, Sumanta N Pattanaik, and Donald P Greenberg. A perceptually based physical error metric for realistic image synthesis. In *Proceedings of the 26th annual conference on Computer graphics and interactive techniques*, pages 73–82. ACM Press/Addison-Wesley Publishing Co., 1999.

[53] Joaquim Salvi, Jordi Pages, and Joan Batlle. Pattern codification strategies in structured light systems. In *Pattern recognition*, volume 37, pages 827–849. Elsevier, 2004.

[54] Vignesh Sankar, Ahmed Gawish, and Paul Fieguth. Impact of training images on radiometric compensation. In *Journal of Computational Vision and Imaging Systems*, volume 3.1, 2017.

[55] Giovanna Sansoni, Sara Lazzari, Stefano Peli, and Franco Docchio. 3D imager for dimensional gauging of industrial workpieces: state of the art of the development of a robust and versatile system. In *3-D Digital Imaging and Modeling, 1997. Proceedings., International Conference on Recent Advances in*, pages 19–26. IEEE, 1997.

[56] RM Shapley and DJ Tolhurst. Edge detectors in human vision. In *The Journal of physiology*, volume 229, pages 165–183. Wiley Online Library, 1973.

[57] Gaurav Sharma, Wencheng Wu, and Edul N Dalal. The ciede2000 color-difference formula: Implementation notes, supplementary test data, and mathematical observations. In *Color Research and Application*, volume 30.1, pages 21–30. Wiley Online Library, 2005.

[58] Christian Siegl, Matteo Colaianni, Marc Stamminger, and Frank Bauer. Adaptive stray-light compensation in dynamic multi-projection mapping. In *Computational Visual Media*, volume 3, pages 263–271. Springer, 2017.

[59] Jun Tsukamoto, Daisuke Iwai, and Kenji Kashima. Radiometric compensation for cooperative distributed multi-projection system through 2-DOF distributed control. In *IEEE transactions on visualization and computer graphics*, volume 21, pages 1221–1229. IEEE, 2015.

[60] Dong Wang, Imari Sato, Takahiro Okabe, and Yoichi Sato. Radiometric compensation in a projector-camera system based properties of human vision system. page 100. IEEE, 2005.

[61] Ting-Chun Wang, Tai-Hsiang Huang, and Homer H Chen. Radiometric compensation for procam system based on anchoring theory. In *Image Processing (ICIP), 2013 20th IEEE International Conference on*, pages 103–107. IEEE, 2013.

[62] Zhou Wang, Alan C Bovik, Hamid R Sheikh, and Eero P Simoncelli. Image quality assessment: from error visibility to structural similarity. In *IEEE Transactions on Image Processing*, volume 13.4, pages 600–612. IEEE, 2004.

[63] Georg Wiora. High-resolution measurement of phase-shift amplitude and numeric object phase calculation. In *Vision Geometry IX*, volume 4117, pages 289–300. International Society for Optics and Photonics, 2000.

[64] Takenobu Yoshida, Chinatsu Horii, and Kosuke Sato. A virtual color reconstruction system for real heritage with light projection. In *Proceedings of VSMM*, volume 3, 2003.